Science Arts & Métiers (SAM)

is an open access repository that collects the work of Arts et Métiers Institute of Technology researchers and makes it freely available over the web where possible.

This is an author-deposited version published in: https://sam.ensam.eu
Handle ID: .http://hdl.handle.net/10985/23801

To cite this version :

Lei SHI, Desheng ZHANG, Annie-Claude BAYEUL-LAINÉ, Olivier COUTIER-DELGOSHA - Effect of pitching angle, pitch-pivot-point, blade camber and deflected sharp leading edge on performance and vortical flows of reversed pitching airfoils - Ocean Engineering - Vol. 280, p.114637 - 2023

Any correspondence concerning this service should be sent to the repository Administrator : scienceouverte@ensam.eu

Arts et Métiers Institute of Technology

Effect of pitching angle, pitch-pivot-point, blade camber and deflected sharp leading edge on performance and vortical flows of reversed pitching airfoils

Lei Shi [a,b], Desheng Zhang [a,*], Annie-Claude Bayeul-Lainé [b], Olivier Coutier-Delgosha [b,c]

[a] Research Center of Fluid Machinery Engineering and Technology, Jiangsu University, Zhenjiang, 212013, China
[b] Arts et Métiers ParisTech, ONERA, CNRS, Univ. Lille, Centrale Lille, UMR 9014-LMFL-Laboratoire de Mécanique des Fluides de Lille-Kampé de Fériet, F-59000, Lille, France
[c] Kevin T. Crofton Department of Aerospace and Ocean Engineering, Virginia Tech, Blacksburg, VA, 24060, USA

A B S T R A C T

The goal of the present work is to investigate the influence of several parameters on the performance and flow structures of reversed pitching airfoils. Firstly, the effect of the turbulence model is evaluated, and the results show that the SST $\gamma - \widetilde{Re}_{\theta t}$ transition model has a better prediction in the instantaneous lift coefficient of a reversed pitching airfoil and the transition locations of a stationary airfoil. Then, effects of the pitching angle, pitch-pivot-point, blade profile and morphed leading edge with various deflection angles and positions on the performance, unsteady vortical flow, near-wall transition and trajectory of main vortices, are analyzed. The main results show that both the mean pitching angle and pitching amplitude have the impact on the vortical flows, but depends on the reduced frequency. Then, the delayed flow structure by shifting the pitch-pivot-point from the leading edge (LE) to trailing edge (TE) can be explained by the distribution of the effective attack-of-angle. Moreover, the symmetrical, asymmetrical and inverse asymmetrical airfoils have great effect on the first (FMLC) and second maximal lift coefficients (SMLC). Finally, upward deflected LE decreases the negative lift coefficient while downward morphed LE improves it considerably due to the geometry curvature leading to the large flow separation. In addition, it is observed that the generation of vortices is earlier when the deflection position close to the middle surface. It is believed that this work can provide some guidelines to have a better design of energy devices with oscillating airfoils/hydrofoils.

1. Introduction

Oscillating airfoils have been widely applied to many engineering equipment, involving vertical-axis wind turbines, micro air vehicles and underwater propulsion system. The motion mode of oscillating foils can be generally classified into three categories: plunging (or heaving), pitching and flapping (combination of the heaving and pitching), which shows the crucial effect on the aero/hydrodynamic performance and flow structures (Wu et al., 2020). The pure pitching motion refers to the target undergoing the process of the up-stroke and down-stroke in a cycle, based on a pitch-pivot-point along the blade chord line. Until now, there are lots of works focusing on the parametrical study of pitching foils, mainly involving the reduced frequency (Guillaud et al., 2018; Amiralaei et al., 2010), pitching amplitude (Lu et al., 2013; Rahromostaqim et al., 2016), pitching location (Li et al., 2019; Tian et al., 2016a), Reynolds number (Kim and Chang, 2014; Hillenherms et al., 2004), pitching kinematic (Lu et al., 2013; Chao et al., 2019) and blade camber (Lu et al., 2013; Mamouri et al., 2019). In vertical-axis turbines or propellers, the blade would experience the advancing and retreating sides, characterized by the fully different foil geometry placement. At retreating side, the blade operates in reversed mode as the sharp TE becomes LE, which displays a totally different characteristic compared with forward foils.

As stated in the aforementioned investigation, the pitch-pivot-point has an evident impact on the force generation, leading-edge vortex (LEV) and wake vortices. Granlund et al. (2011) compared pitching flat plates with different pitching locations and the main conclusion is that the LEV development is delayed as the pitch-pivot-point moves to TE.

* Corresponding author. Research Center of Fluid Machinery Engineering and Technology, Jiangsu University, Zhenjiang, 212013, China.
E-mail address: zds@ujs.edu.cn (D. Zhang).

Tian et al. (2016a) experimentally investigated the influence of the pitching location on the propulsive performance of a pitching airfoil, and found that the circulation and transverse spacing of wake vortices are increased when the pitch-pivot-point is closer to LE under the same reduced frequency condition. Furthermore, Yu and Bernal (2017) studied the effect of the pitch-pivot-point on a pitching rectangle flat plate and observed that the LEV develops earlier when the pitching location approaches to LE. Actually, changing the pitch-pivot-point would modify the effective attack-of-angle, which further affects the performance and flow structure. Tian et al. (2016a) concluded that moving the pitch-pivot-point is equal to add a plunging motion compared with the original pitching case, which is beneficial to the generation of the additional thrust force. Thus, Li et al. (2019) proposed a novel way to improve the lift of a pitching airfoil with a movable pitch-pivot-point. Additionally, the blade profile is one of important parameters that has an influence on the performance and flow structure of oscillating foils. Although Lu et al. (2013) clarified that the mean thrust of different blade profiles are almost unchanged, the instantaneous distributions of the thrust and power coefficients vary considerably. McCroskey et al. (1981) compared the performance and dynamic stall of eight profiles and observed that six modern sections are superior to the original NACA0012 airfoil. In addition, the airfoils with better static-stall characteristics seem to have better dynamic-stall behaviour sometimes. Recently, Benton and Visbal (2018) found that increasing the leading-edge radius and the addition of the leading-edge droop can delay the dynamic stall.

There are some works performed on stationary and oscillating reversed airfoils/hydrofoils, with the main focus on the parametrical study of the performance and flow structure. With the application to the tidal turbine, Marchand et al. (2017) observed that there is a discontinuity of the lift at zero degree, because of the leading-edge separation bubble and the inherent asymmetry of the boundary layer. With the increase of the incidence, Lind and Jones (2016a) found that unsteady loads and flow structures of reversed airfoils exhibit different features, and NACA0012 in reverse flow is insensitive to the Reynolds number due to the flow separation at the sharp LE. This event is also reported by Lind et al. (2016), and they also observed that the reversed NACA0024 shows a decrease of airloads with the increase of the Reynolds number when the incidence is below 15°. When considering the blade camber effect, Lind et al. (2014) and Lind and Jones (2015) stated that the drag of the reversed NACA0012 is much larger than that of the elliptical airfoil, and separation occurs earlier near the sharp LE for NACA0012. Then, when the airfoil has a pitching motion, Hodara et al. (2016) used both the high-fidelity computations and experiments to capture the general vortices, involving the convection and growth of the dynamic stall vortex, a trailing-edge vortex (TEV) and a secondary dynamic stall vortex. However, the simulation underpredicts the size and strength of TEV, without the consideration of the blockage in the experiments. Moreover, Lind and Jones (2016b) found that the reduced frequency strongly affects the onset and persistence of the dynamic stall vortex, and the number of the vortex increases with the decrease of the reduced frequency and increase of the maximal pitching angle.

Until now, to enhance the performance of airfoils with different applications, lots of flow control methods are employed, such as the leading-edge protuberances (Hansen et al., 2011; Seyhan et al., 2022), vortex generators (Kundu, 2020; Seshagiri et al., 2009), Gurney flaps (GF) (Cole et al., 2013; Wang et al., 2008) and so on. The leading-edge tubercles allow the flow to remain attached in a wide range of incidences, leading to the delay of the stall and lift enhancement (Hansen et al., 2011). Then, the application of the vortex generators aims to energize the sluggish boundary layer, to delay the flow separation and increase the maximal lift coefficient. However, it also shows that the vortex generator can increase the minimum drag and decrease the lift-to-drag ratio (Seshagiri et al., 2009). Furthermore, as a lift-enhancement device, the GF with a small size located near the TE can increase the maximal lift a lot, due to the increase of the pressure

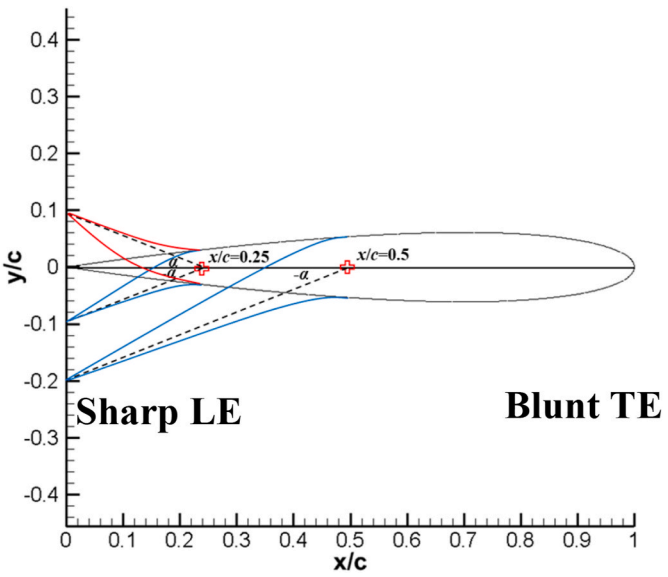

Fig. 1. A reversed airfoil with morphed LE (The red line represents the upward deflection and blue lines are downward morphed camber at different positions).

difference induced by a short separation region around the GF (Cole et al., 2013). Using the morphed leading-edge is another approach to improve the airfoil performance as a result of suppressing the flow separation effectively. For the airfoil in reverse flow, massive flow separation occurs near the sharp LE, which could result in the increase of the drag. Jacobellis et al. (2020) reported that the deflected angle with 10° of the airfoil in reverse flow reduces the drag by 50%, resulting from the absence of the separation bubble near the sharp LE. Ko et al. (2021) also observed that the morphed LE leads to a significant decrease of the separation bubble and wake size, which further causes the large reduction of the drag and pitching moment and a minor reduction of the negative lift. As shown in Fig. 1, it is excepted that the flow separation near the sharp LE is alleviated by using the deflected camber when the airfoil is in reverse flow, to improve the performance more or less.

According to the previous work, it is observed that the parametrical study of the pitching airfoil in reverse flow is still rarely investigated, and the underlying flow physics under different parameter conditions are not understood well. Consequently, the main objective of the present work can be divided into two parts: (1) studying the influence of the pitching angle, pitch-pivot-point and blade camber; (2) proposing a flow control method by using the morphed LE. The main emphasis is on the analysis of the performance, boundary layer flows and vortex dynamics of reversed pitching airfoils under different parameter conditions. This work can provide the inspiration to design a high-performance vertical-axis turbines and propellers.

2. Problem description

2.1. Computational configuration and meshing

The baseline airfoil used in this work is NACA0012 with a chord of $c = 0.203$m, and the corresponding Reynolds number is about 1.65×10^5. The turbulence model used here is SST $\gamma - \widetilde{Re}_{\theta t}$ transition model, which was initially proposed by Menter et al., 2006a, 2006b. As shown in Fig. 2a, the computational configuration is a rectangle section, in which the inlet part extends $5c$ from the airfoil sharp LE and the outlet is located at $x = 10c$ from the blunt TE. Due to the quick dissipation of the wake flow, the length of the outlet section is sufficient in this work. The top-wall and bottom-wall have the distance of $4c$ from the pitching point, which locates at $x/c = 0.75$ consistent with the experimental setup. The airfoil operates with a sinusoidal motion, involving a mean

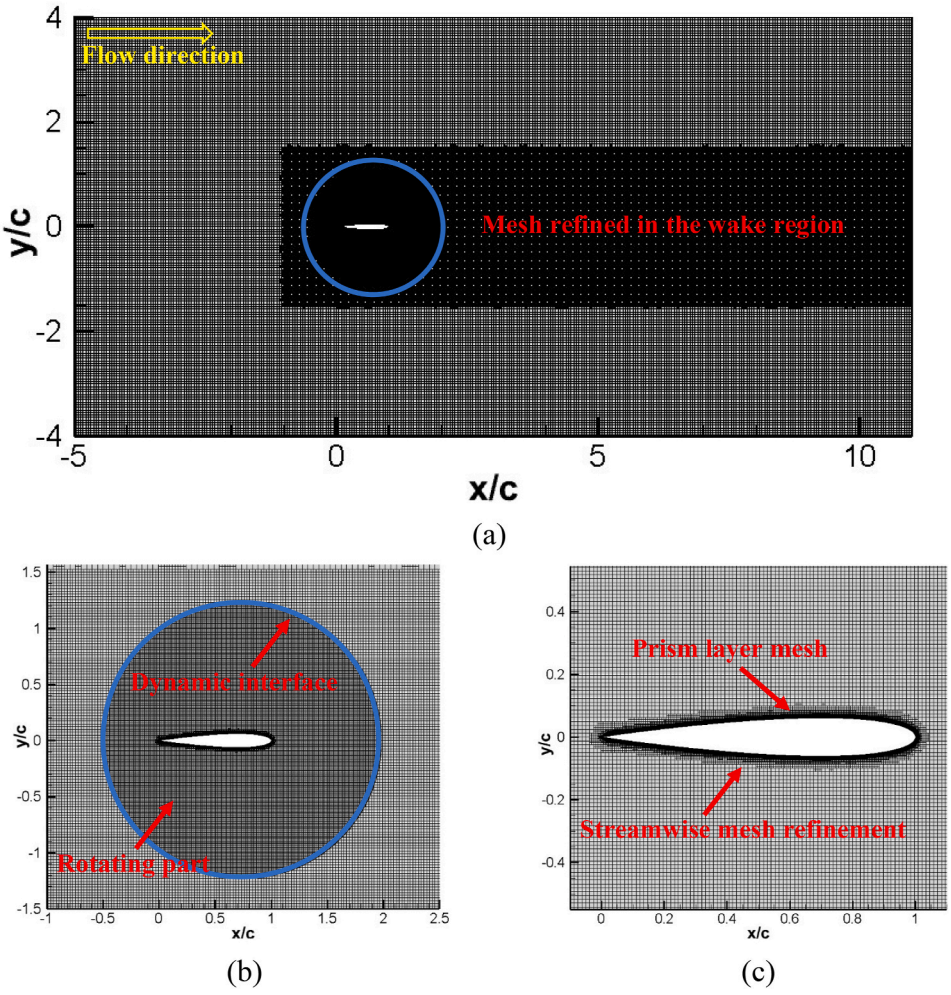

Fig. 2. Computational domain and mesh arrangement. (a) Computational domain; (b) Mesh in the rotating part; (c) Mesh near the airfoil surface.

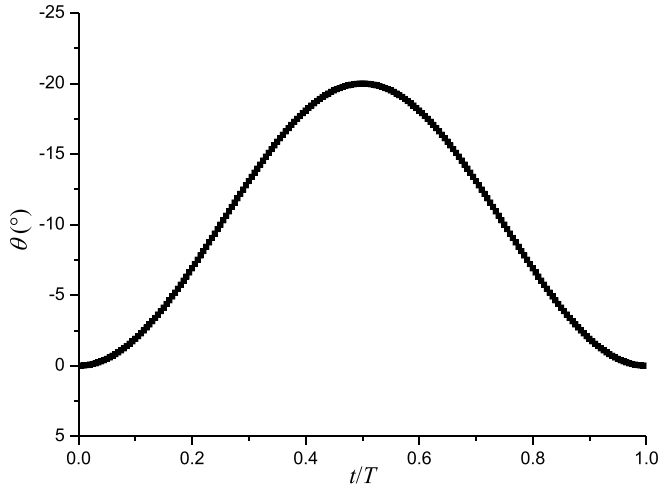

Fig. 3. Pitching kinematic of the reversed pitching airfoil.

pitching angle of -10° and a pitching amplitude of 10°. The oscillating frequency is about 3Hz, achieving a reduced frequency $k = \pi fc/U_0 = 0.16$ (f is the pitching frequency and U_0 is the freestream velocity). The incidence variation for the reversed pitching airfoil is plotted in Fig. 3.

The mesh arrangement of the computational domain is displayed in Fig. 2. The sliding mesh is used to control the airfoil movement by establishing a rotating part. Then, a cylinder including the rotating part is created, to refine the mesh in the wake region. To study the influence of the streamwise mesh, the airfoil surface mesh size is decreased gradually. In addition, by decreasing the number of the prism layer and prism layer total thickness, the effect of the mesh in the normal direction is also investigated. The prism layer stretching ratio keeps a constant value of 1.1 and the size of the refined mesh in the wake region remains unchanged for all tested cases. The detailed information about the mesh distribution is listed in Table 1. In Fig. 4, the lift coefficients in a pitching cycle obtained by different meshes are presented and the numerical result is compared with the experiment (Hodara et al., 2016). It seems that before $t/T = 0.55$, the computation captures the performance

Table 1
Detailed information of the mesh arrangement.

	Mesh size of the rotating part (mm)	Number of the prism layer	Prism layer thickness (mm)	Mesh size around the surface (mm)	Total cells
Mesh 1	5	50	5	0.8	136,152
Mesh 2	4	55	4	0.6	153,893
Mesh 3	2	60	2.5	0.4	208,957
Mesh 4	1.5	65	2	0.2	221,663

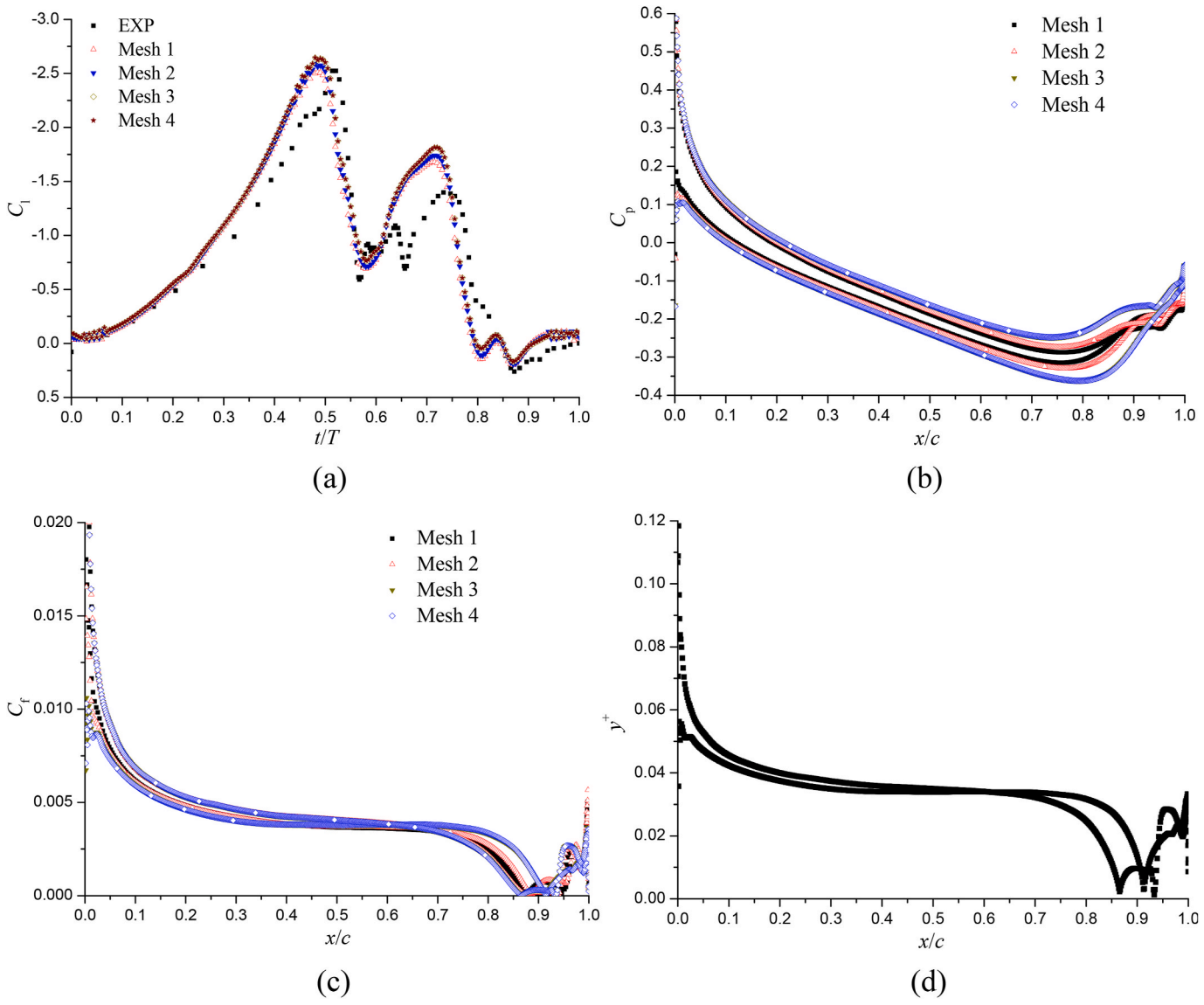

Fig. 4. Variables obtained by different meshes. (a) Lift coefficient; (b) Pressure coefficient; (c) Skin friction coefficient; (d) $y^+$for mesh 3.

change well, but the discrepancy becomes relatively large when the airfoil pitches up ($0.5< t/T < 1.0$). Martinat et al. (2008) reported that the downstroke stage of the forward airfoil ($0.5< t/T < 1.0$) is strongly related to three-dimensional flows along the span, while the flow is practically two-dimensional during the upstroke motion. It is observed that the results including the lift coefficient (C_l=F_L/(0.5*ρ*U_0^2), F_L is the lift), pressure coefficient ($C_p = p/(0.5*\rho*U_0^2)$, p is the pressure) and skin friction coefficient ($C_f = \tau/(0.5*\rho*U_0^2)$, τ is the magnitude of the wall shear stress), are almost unchanged for mesh 3 and 4, which indicates that the flow is fully resolved. For mesh 3, the y^+ ($y^+ = yu_\tau/\nu$, y is the distance to the wall, u_τ is the friction velocity and ν is the kinematic viscosity) distribution is displayed in Fig. 4d. The maximal value is near the sharp LE, where the flow separation exists. Additionally, the y^+ on most part of the surface is below 0.06, indicating that the present simulation has the capability to resolve the boundary layer flow.

2.2. Boundary conditions and numerical setup

The two-dimensional incompressible unsteady flow is solved by the commercial code STARCCM+. In the simulation, the classical boundary condition was employed: the constant velocity is imposed on the inlet section while the pressure is assigned on the outlet region. The 2nd-order upwind scheme is employed to the convection term while the 2nd-order Backward Euler scheme is applied to the temporal discretization. The wall function used here is all y^+wall treatment, which uses the low y^+ wall treatment for fine meshes, and high y^+ wall treatment for coarse meshes. Thus, this wall treatment is suitable for a wide range of near-wall mesh densities. The time-step is set as $t = T/200$s, which is validated in our previous work (Shi et al., 2022). In order to eliminate the time effect, 15 rotations are adopted for each case, and flow structures in the last rotation are used to analyze the performance change.

3. Results and discussion

3.1. Validation of the numerical result

The choice of the turbulence model is critical to the prediction of the performance. Rezaeiha et al. (2019) tested a series of RANS-based turbulence models to predict the performance of vertical-axis wind turbines, and concludes that the transitional SST k-ω versions are recommended in the transitional flow regime. Zhang et al. (2020) used the SST $\gamma - \widetilde{Re}_{\theta t}$ transition model to investigate the influence of the reduced frequency k on the hydrodynamic performance of a pitching

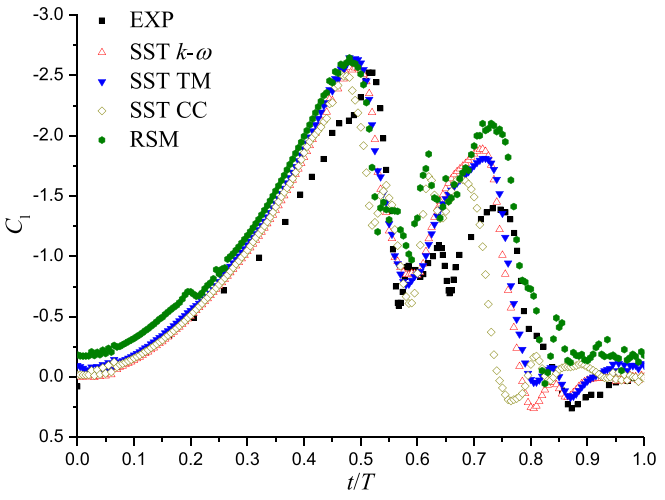

Fig. 5. Instantaneous lift coefficients obtained by different turbulence models.

hydrofoil, and a good agreement is observed compared with the experiments. Thus, four different turbulence models, including the original SST k-ω model (Menter et al., 2003), SST $\gamma - \widetilde{Re}_{\theta t}$ transition model (SST TM) (Menter et al., 2006a, 2006b), SST k-ω model with curvature correction (SST CC) (Shur et al., 2000) and Reynolds stress model (RSM) (Durbin, 1993), are tested. In Fig. 5, it is found that the evolution of the lift coefficient achieved by SST TM is closer to the experimental data. Although the results of SST k-ω model, SST TM and SST CC are quite close in the down-stroke process ($0< t/T < 0.5$), there exists large difference in the up-stroke motion. For an example, from $t/T = 0.75$–1.0, it is obvious that the lift coefficient variation produced by SST TM has a relatively small error. In addition, the SST CC predicts a worse performance compared with other two models. The performance achieved by RSM is quite noisy, especially in the upstroke motion, possibly due to the unsteadiness of the flow structure caused by the solution of many variables in the equations. In general, it concludes that the SST TM has a better prediction of the lift coefficient for the reversed pitching airfoil, but how to get a more accurate estimation of the performance in the upstroke stage still needs to be investigated.

In Fig. 6, the instantaneous flow structures at different instants obtained by SST TM are compared with PIV (Particle Image Velocimetry) measurements (Hodara et al., 2016). At $t/T = 0.32$, the LEV develops along the lower surface. When the dynamic stall occurs at $t/T = 0.53$, the LEV starts to shed from the surface, while the TEV emerges near the blunt TE. At the same time, near the sharp LE, the second LEV (SLEV) and a vortex A coexist. This event was also reported by Tseng and Hu (2016), who observed that a reverse flow from the lower surface of the forward airfoil and the fluid flow around the outer edge of the LEV form this special structure. Then, as the incidence becomes small at $t/T = 0.61$, the SLEV moves towards the middle surface, while the TEV begins to shed into the wake, leading to the lift drop significantly, which can be observed in Fig. 5. In general, before the occurrence of the dynamic stall, the flow structure evolution predicted by the simulation has a good agreement with the experiment. However, once the dynamic stall appears or the airfoil undergoes the up-stroke process, the discrepancy becomes relatively large, which is also shown by the distribution of the lift coefficient in Fig. 5.

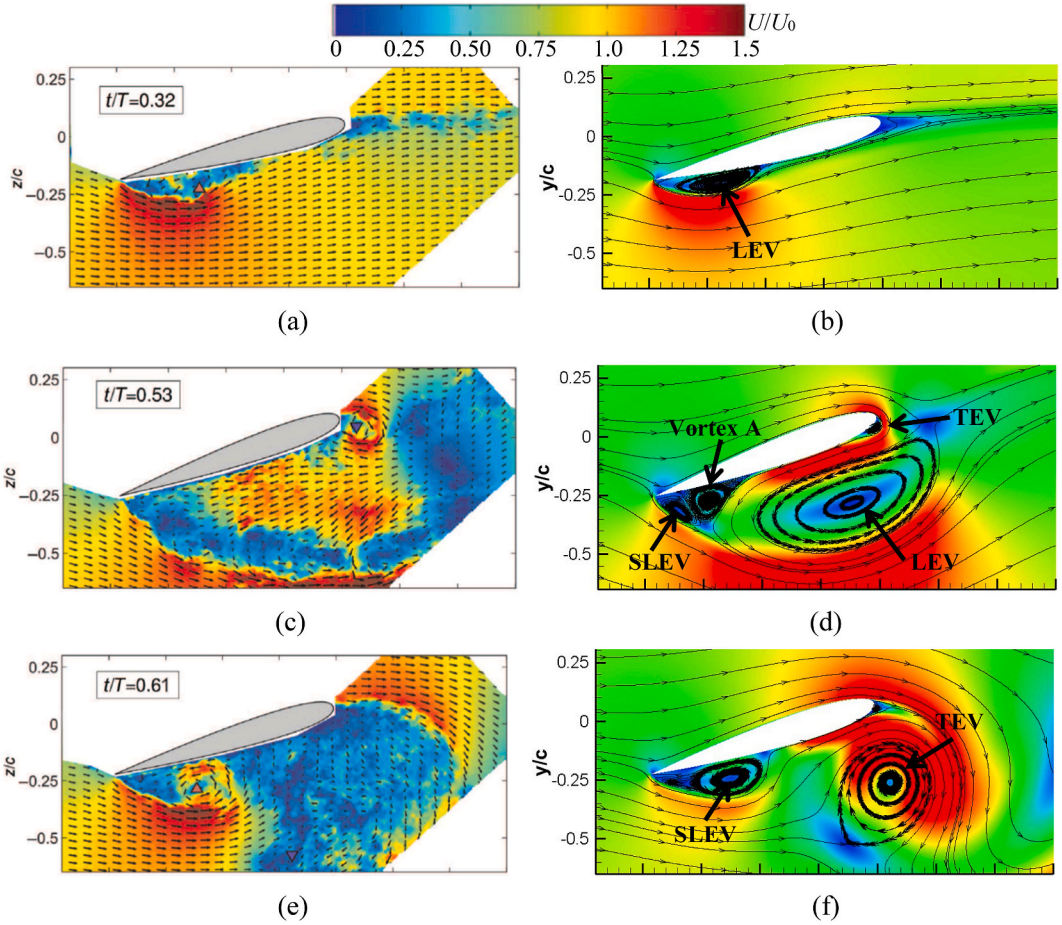

Fig. 6. Instantaneous flow structures at different instants. (a) $t/T = 0.32$ (EXP); (b) $t/T = 0.32$ (NUM); (c) $t/T = 0.53$ (EXP); (d) $t/T = 0.53$ (NUM); (e) $t/T = 0.61$ (EXP); (f) $t/T = 0.61$ (NUM).

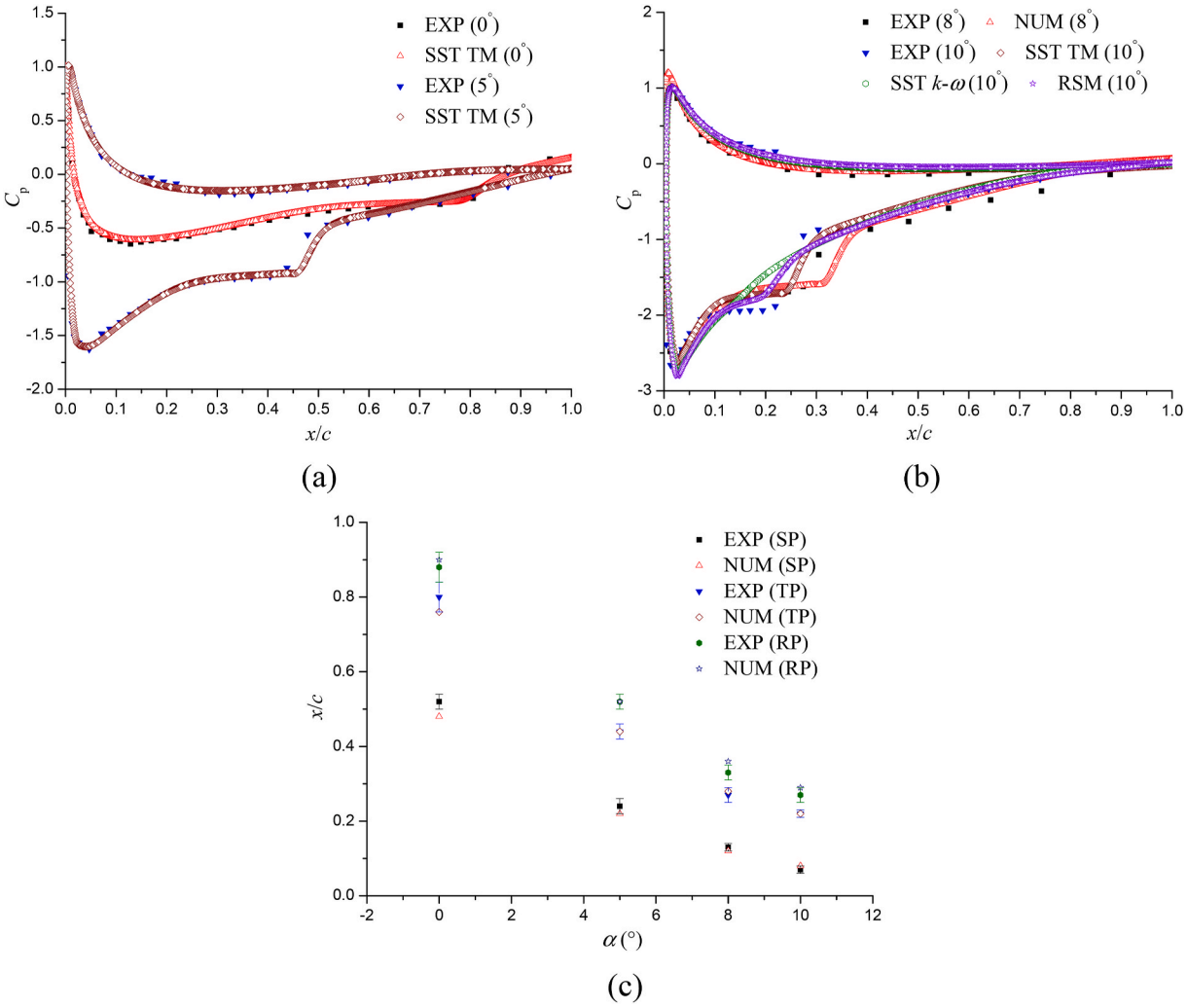

Fig. 7. Mean pressure coefficients and transition locations at different incidences. (a) Pressure coefficients at $\alpha = 0^{\circ}$ and 5°; (b) Pressure coefficients at $\alpha = 8^{\circ}$ and 10°; (c) Separation, transition and reattachment points.

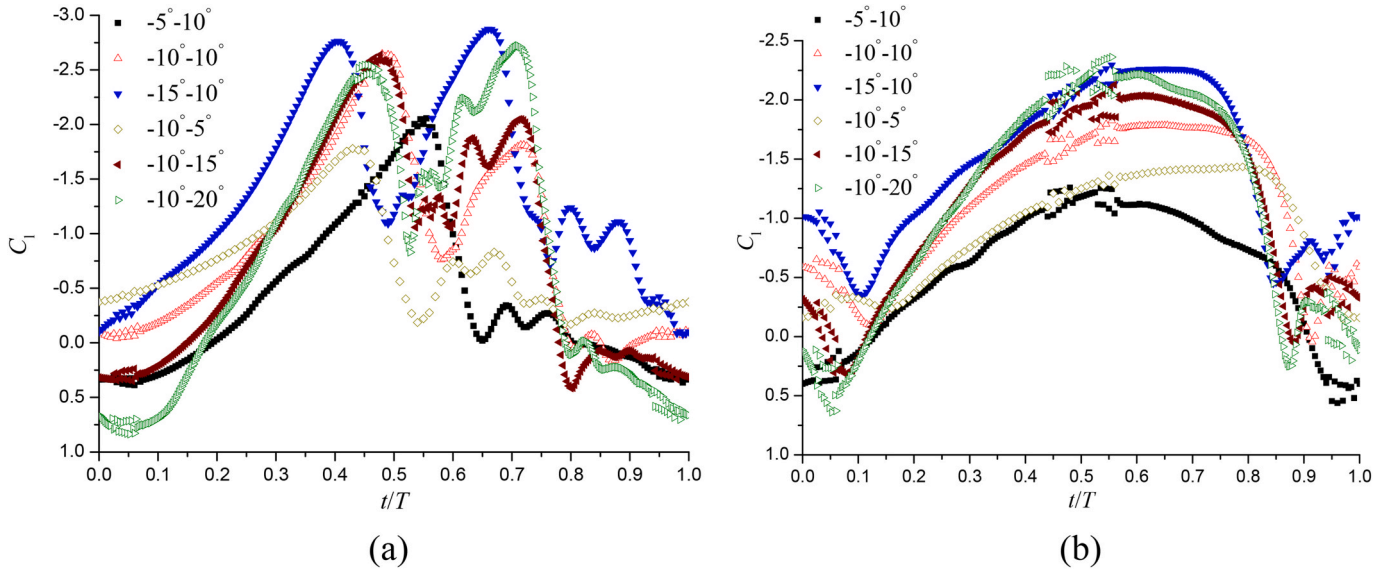

Fig. 8. Instantaneous lift coefficients of different cases at two k. (a) $k = 0.16$; (b) $k = 0.50$.

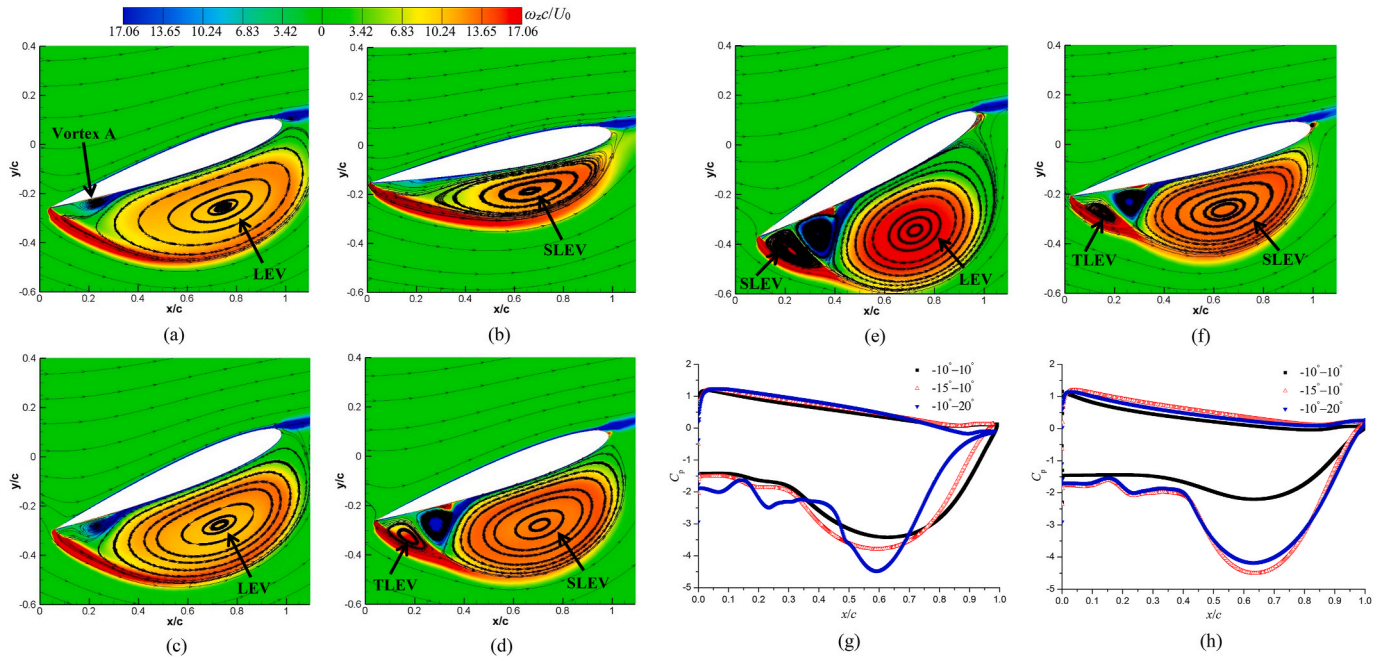

Fig. 9. Flow structures and pressure coefficients of different cases at $k = 0.16$. (a) -10°–10° at $t/T = 0.49$; (b) -10°–10° at $t/T = 0.72$; (c) -15°–10° at $t/T = 0.4$; (d) -15°–10° at $t/T = 0.66$; (e) -10°–20° at $t/T = 0.46$; (f) -10°–20° at $t/T = 0.70$; (g) FMLC; (h) SMLC.

At low Reynolds number, the laminar-turbulence transition is an event that can't be neglected. At relatively low incidence, the flow-separation induced transition due to the existence of a laminar separation bubble (LSB) has great impact on the performance, which should be considered in the present work. Because of the infrequent data about the transition on the oscillating airfoils, the transitional flows over a stationary airfoil NACA 0018 at $\mathrm{Re} = 1 \times 10^5$ are investigated at different incidences. Fig. 7 presents the time-averaged pressure coefficients and transition locations at different incidences. It is observed that at 0° and 5°, the pressure coefficients of tested cases have good agreement with the experiments (Kirk and Yarusevych, 2017). When the incidence increases to 8° and 10°, the error becomes large gradually, especially near the transition region. At 10°, the other two models, namely SST k-ω model and RSM, are also adopted to evaluate the turbulence model effect. The results show that the SST k-ω model only resolves the fully turbulent flow. Although RSM performs better than the SST k-ω model, it underpredicts the size of the transition region. By the comparison, it concludes that SST TM indeed has the superiority to predict the transitional flow near the wall. Then, in Fig. 7c, the prediction of the separation (SP), transition (TP) and reattachment points (RP) by SST TM matches the experiments well.

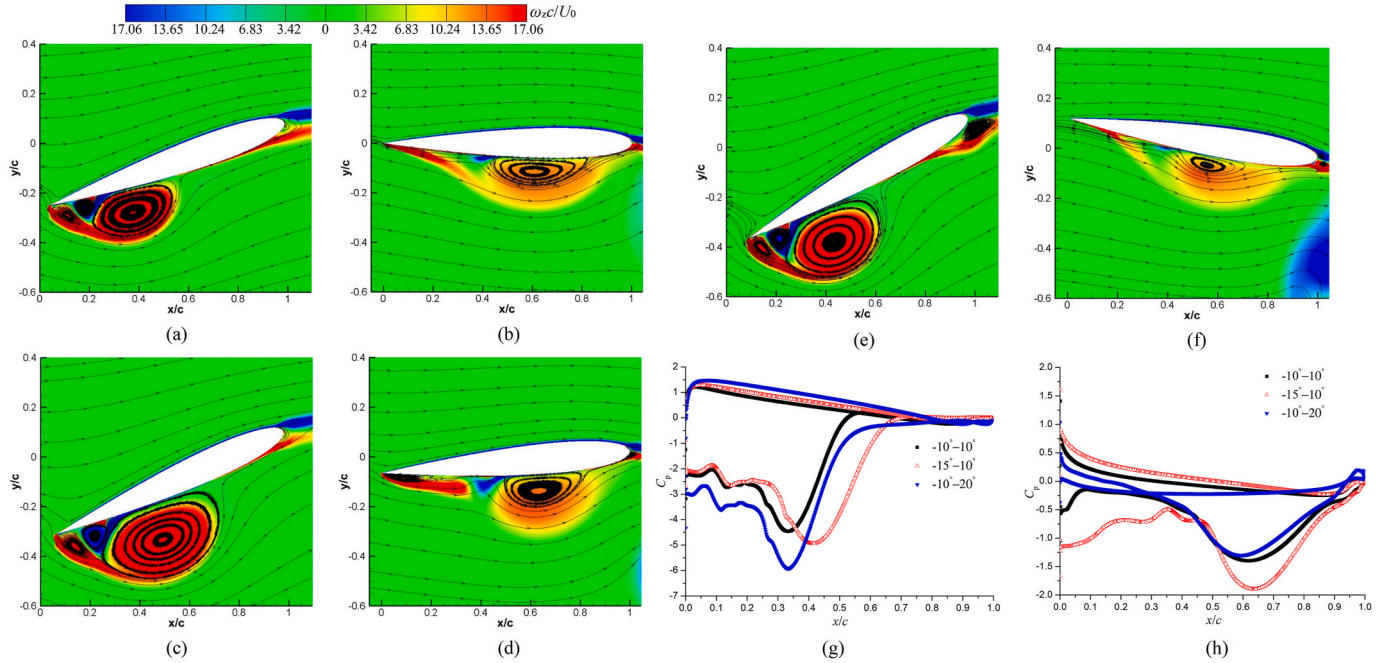

Fig. 10. Flow structures and pressure coefficients of different cases at $k = 0.50$. (a) -10°–10° at $t/T = 0.55$; (b) -10°–10° at $t/T = 1.0$; (c) -15°–10° at $t/T = 0.55$; (d) -15°–10° at $t/T = 1.0$; (e) -10°–20° at $t/T = 0.55$; (f) -10°–20° at $t/T = 0.95$; (g) FMLC; (h) SMLC.

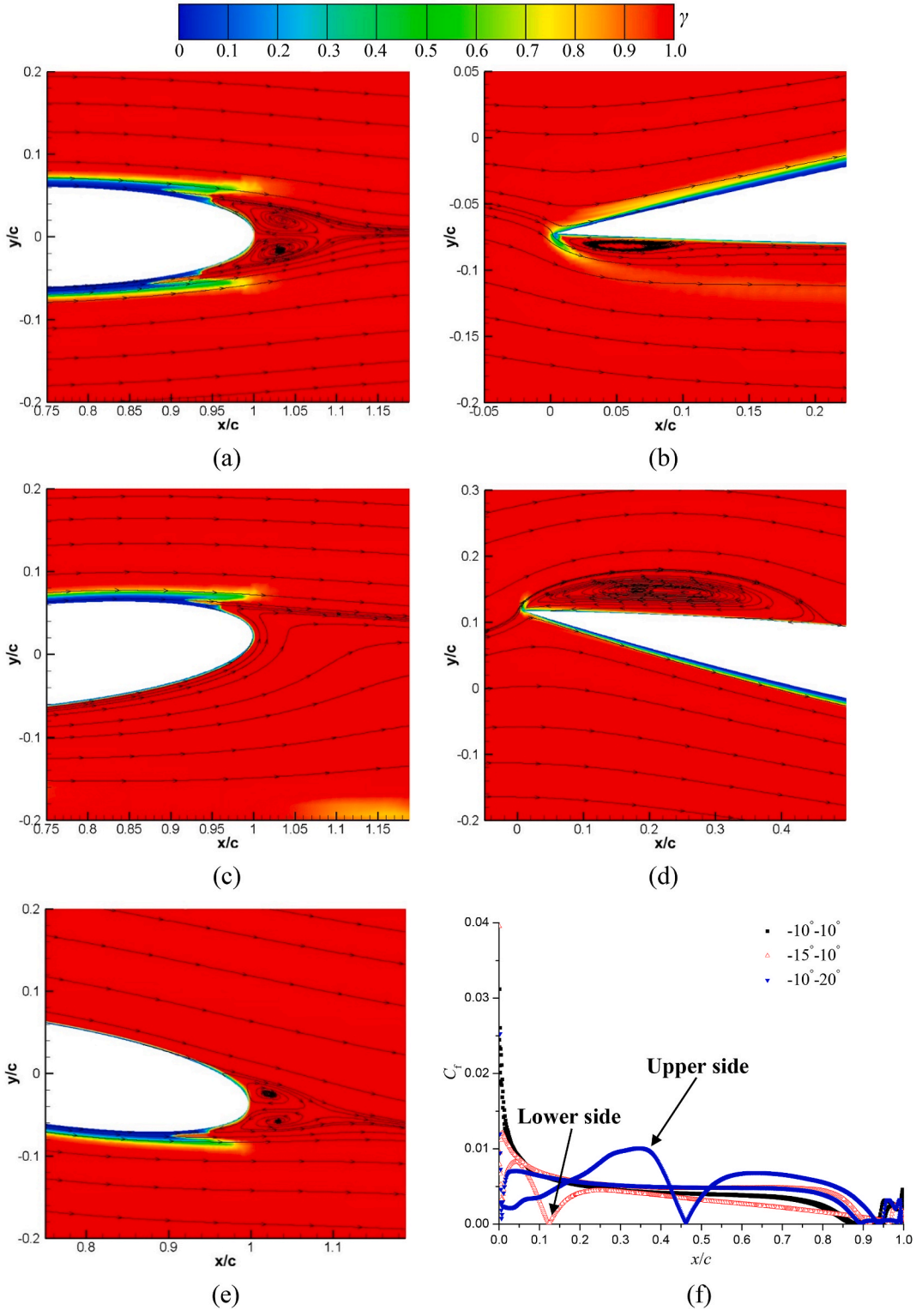

Fig. 11. Near-wall flows and skin friction coefficients of different cases at $k = 0.16$. (a) -10°–10° (TE); (b) and (c) -15°–10° (LE and TE); (d) and (e) -10°–20° (LE and TE); (f) Skin friction coefficients.

3.2. Effect of the pitching angle on the reverse flow

Several cases with various mean pitching angles and pitching amplitudes at $k = 0.16$ and 0.50, are employed. The instantaneous lift coefficients in a revolution for different cases are plotted in Fig. 8, in which '-5°–10°'represents the combination of the mean pitching angle and pitching amplitude. The main results show that increasing the mean pitching angle leads to the earlier occurrence and strong intensity of the LEV and SLEV, which is presented by two locations where the negative lift coefficients have the maximal magnitude. Besides, with the increase of the pitching amplitude, the value of the lift coefficient induced by the LEV increases, especially from 5° to 10°. However, when the pitching amplitude increases from 10° to 20°, the lift coefficient at about $t/T = 0.5$ has no much difference, which indicates that the LEV has little influence

on the performance. But at about $t/T = 0.72$, increasing the pitching amplitude can still affect the development of SLEV, increasing the negative lift coefficient evidently.

As k increases to 0.50, it is obvious that the FMLC is postponed compared with that at $k = 0.16$. For the SMLC, it even occurs in the next evolution. Moreover, when the mean pitching angle increases, the magnitude of FMLC increases a lot, but they only have a small change as the pitching amplitude increases from 10° to 20°, which is similar with that at $k = 0.16$. Generally, it concludes that increasing k delays the flow structure, especially at large k, since the SLEV occurs in the next pitching cycle. Increasing the mean pitching angle influences both the LEV and SLEV, but only the SLEV is affected significantly by increasing the pitching amplitude from 10° to a larger incidence at low k.

At $k = 0.16$, the flow structures and pressure coefficients at locations where the first two maximal lift coefficients appear are displayed in Fig. 9. For the case of -10°–10°, the LEV occupies the whole lower surface, leading to the large value of the negative lift coefficient, as shown in Fig. 8a. When the SLEV attaches a large part of the surface, the second peak of the lift coefficient occurs, but its magnitude is smaller than the first one, which indicates that the intensity of SLEV is weaker than LEV. When the mean pitching angle increases to -15°, although the LEV appears earlier, the intensity is comparable compared with the LEV in Fig. 9a, which can also be found from the pressure distribution in Fig. 9g. The second peak of the lift coefficient is mainly induced by the SLEV, a third leading-edge vortex (TLEV) and vortex A. At the same time, the intensity of SLEV is larger than LEV, leading to the higher lift coefficient in Fig. 8a. With the increase of the pitching amplitude, the airfoil has a large variation of the incidence, but the pressure distribution at FMLC is almost the same, further resulting in nearly the same magnitude of the lift coefficients, as shown in Fig. 8a. However, in Fig. 9h, the effect of SLEV on SMLC is more obvious as the pitching amplitude increases.

When k increases to 0.50, the main flow feature is that except for the main vortices on the lower side, the positive and negative vorticity shedding from the lower and upper sides are visible near the blunt TE, and convect downstream with the time, which can be seen in Fig. 10f. By the comparison of the lift coefficient at $k = 0.16$, it seems that the LEV persists for a long time, for an example, from $t/T = 0.50$–0.70 in Fig. 8b, which could delay the development of the SLEV. Increasing the mean pitching angle would make the evolution of LEV earlier, which takes over a large portion of the lower surface. However, at the same instance, only increasing the pitching amplitude could not change the position of LEV, but the intensity. If the LEV develops late, the pressure recovery would compensate the low pressure induced by LEV, as a consequence, the lift coefficient is almost the same for two cases of -15°–10° and -10°–20° at $t/T = 0.55$. When it comes to the SMLC, it can be seen that the TLEV is generated near the sharp LE for the case of -15°–10°, leading to the reduction of the pressure and the improvement of the lift coefficient, as shown in Fig. 10d and h. For other two cases, the influence of SLEV is relatively small, which has little impact on the lift coefficient. Consequently, it concludes that the lift coefficient depends on the near-wall flow structure induced by the variation of the incidence. Increasing k would decrease the peak of the lift coefficient, and delay the development of SLEV due to the long persistence of LEV.

Fig. 11 shows the transition over the surface for different cases at $k = 0.16$ using the intermittency contours. The intermittency is used to modify the production and dissipation terms in the original SST k-ω model, to trigger the transition onset. Normally, in the laminar boundary layer, the intermittency is 0, while it becomes 1 in the fully turbulent boundary layer. In the transition region, it is $0 < \gamma < 1$. At $t/T = 0.05$, the transition mainly occurs near the blunt TE, and the boundary layer flow is nearly symmetrical, characterized by a pair of vortices. For the case of -15°–10°, due to the existence of the LEV, a separated shear layer from the sharp LE induces the transition. After the LEV, the flow would reattach on the lower surface, which can be found from Fig. 11f. Near the TE, due to the incidence, the boundary layer is extremely

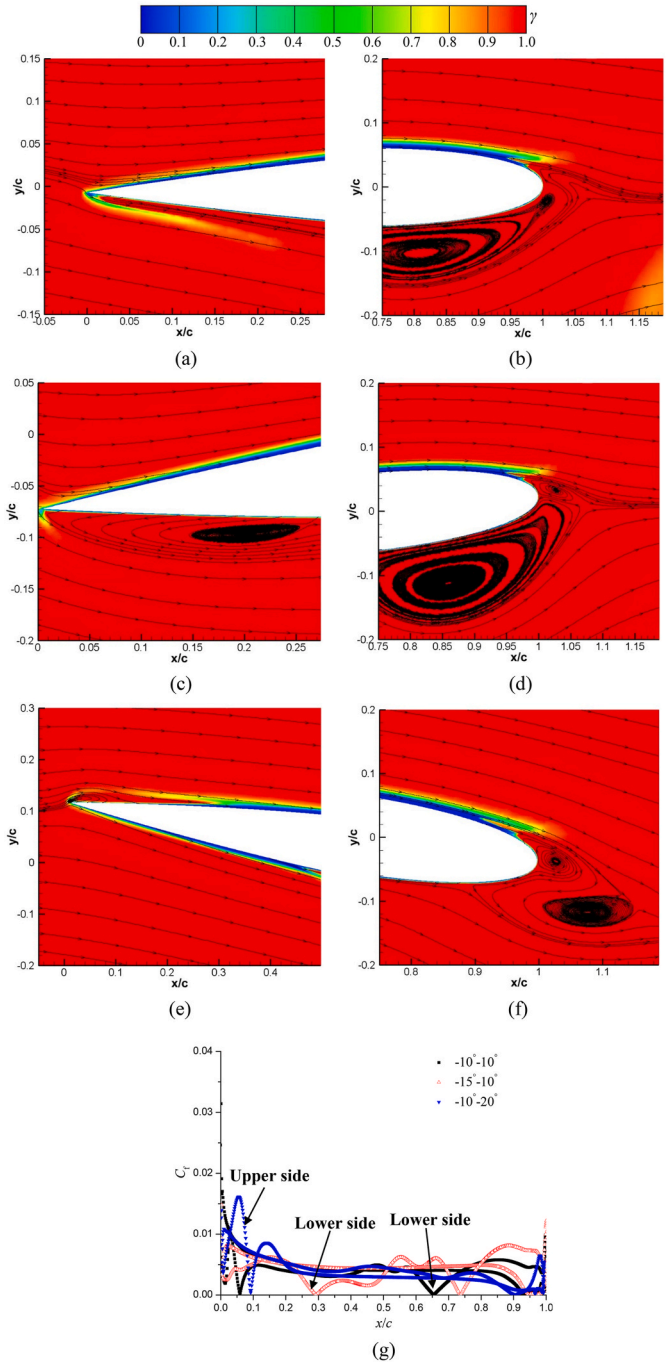

Fig. 12. Near-wall flows and skin friction coefficients of different cases at $k = 0.50$. (a) and (b) -10°–10° (LE and TE); (c) and (d) -15°–10° (LE and TE); (e) and (f) -10°–20° (LE and TE); (g) Skin friction coefficients.

asymmetrical, and the transition mainly appears over the upper surface. Similarly, in Fig. 11d and e, the large-scale LEV is generated on the upper side. Simultaneously, the transition on the lower surface is observed near the TE and a pair of vortices are still visible. Based on the distributions of skin friction coefficients, the location and size of LEV and the transition near TE on both two sides are quite clear.

When $k = 0.50$, at $t/T = 0.05$, the near-wall flows of different cases are displayed in Fig. 12. For the case of -10°–10°, the separated shear layer near the LE is observed while the transition near the TE occurs on the upper surface. Over the lower side, the SLEV still attaches and it interacts with the wake flow. When the mean pitching angle is -15°, due to the relatively large attack-of-angle, the TLEV with large size is

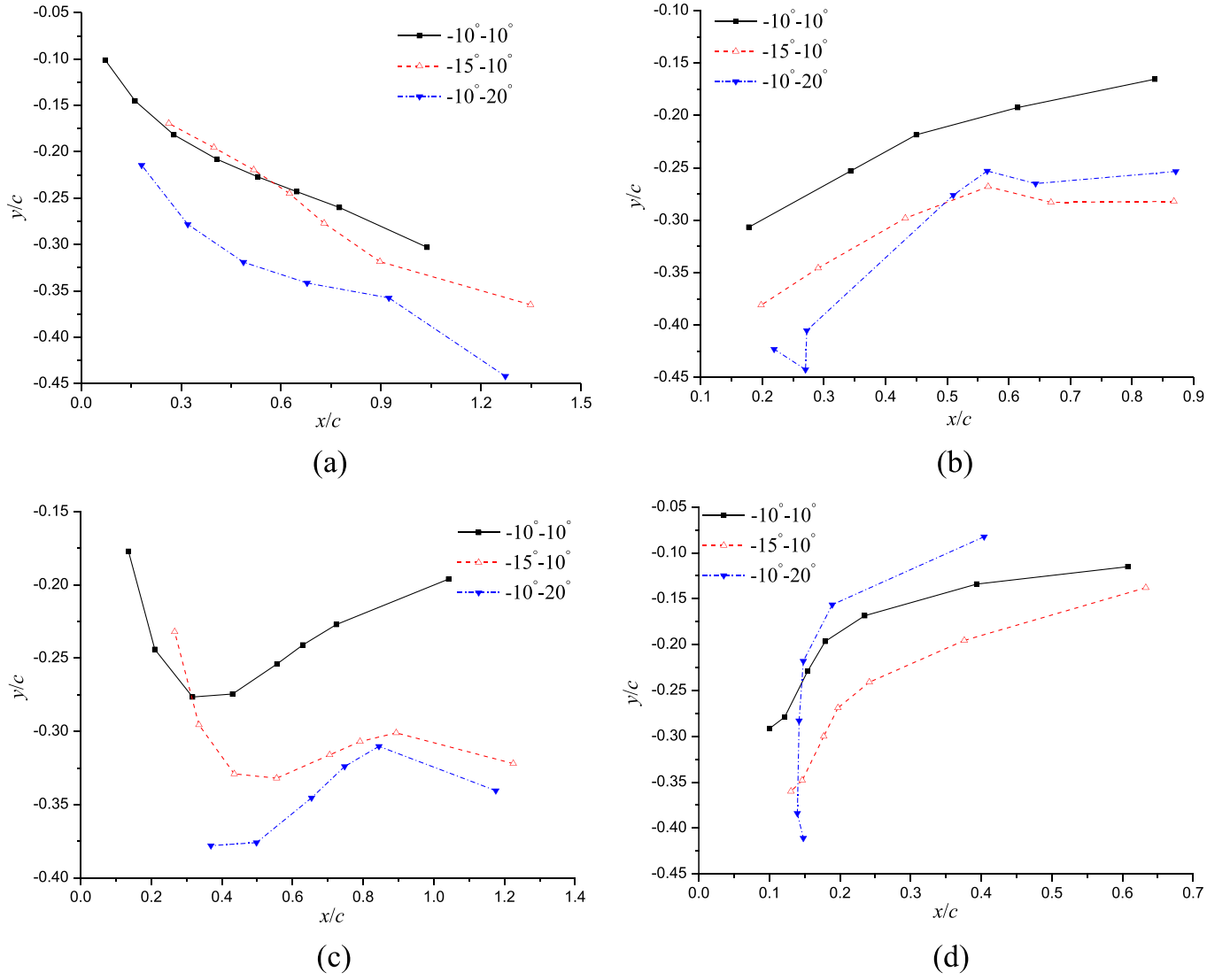

Fig. 13. Trajectory of LEV and SLEV of different cases. (a) LEV at $k = 0.16$; (b) SLEV at $k = 0.16$; (c) LEV at $k = 0.50$; (d) SLEV at $k = 0.50$.

generated and then the flow would reattach. At the same time, the SLEV moves more downstream compared with that in Fig. 12b. When the airfoil has a positive incidence, shown in Fig. 12e, the flow separation appears on the upper side, and the size of the recirculation region is larger than that in Fig. 12a, based on the reattachment point in Fig. 12g. Near the TE, the SLEV sheds into the wake, making the flow more disordered. It seems that the near-wall flow is more complicated at $k = 0.50$ compared with that at $k = 0.16$, especially near the blunt TE, due to the presence of SLEV interacting with the vortex, leading to the highly asymmetrical boundary layer.

The trajectory of LEV and SLEV by tracing the vortex centre for different cases are plotted in Fig. 13 at two k. It should be noted that the reference coordinate is on the sharp LE when the airfoil has an incidence of 0°, as a result, the position of the vortex is not changed with the oscillation of the airfoil, but is based on the horizontal (x) and vertical (y) axis. At $k = 0.16$, the LEV gradually moves away from the horizontal axis, but it is more obvious for the case with large pitching amplitude. However, the SLEV in the case with -10°–10° is closer to the horizontal axis, due to the relatively low incidence. After the middle region, the SLEV moves along the horizontal axis in the case of -10°–20°. As k increases to 0.50, the motion of LEV is quite different from that at $k = 0.16$. It seems that the LEV convects along the horizontal axis for a long time, especially in the case of -10°–10°. However, in other two cases, the LEV

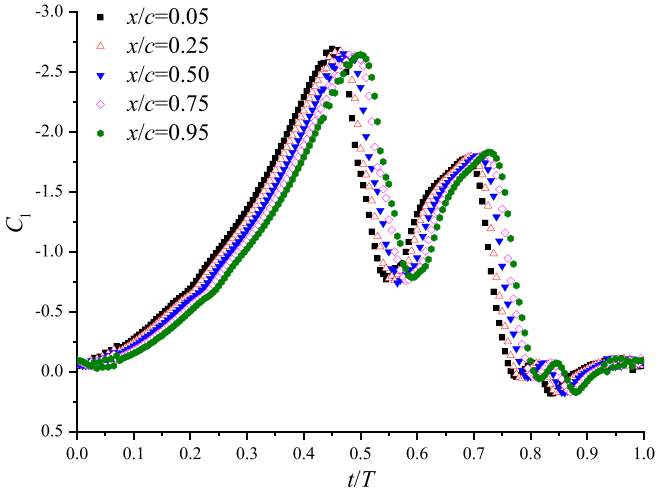

Fig. 14. Instantaneous lift coefficients of airfoils with different pitching locations.

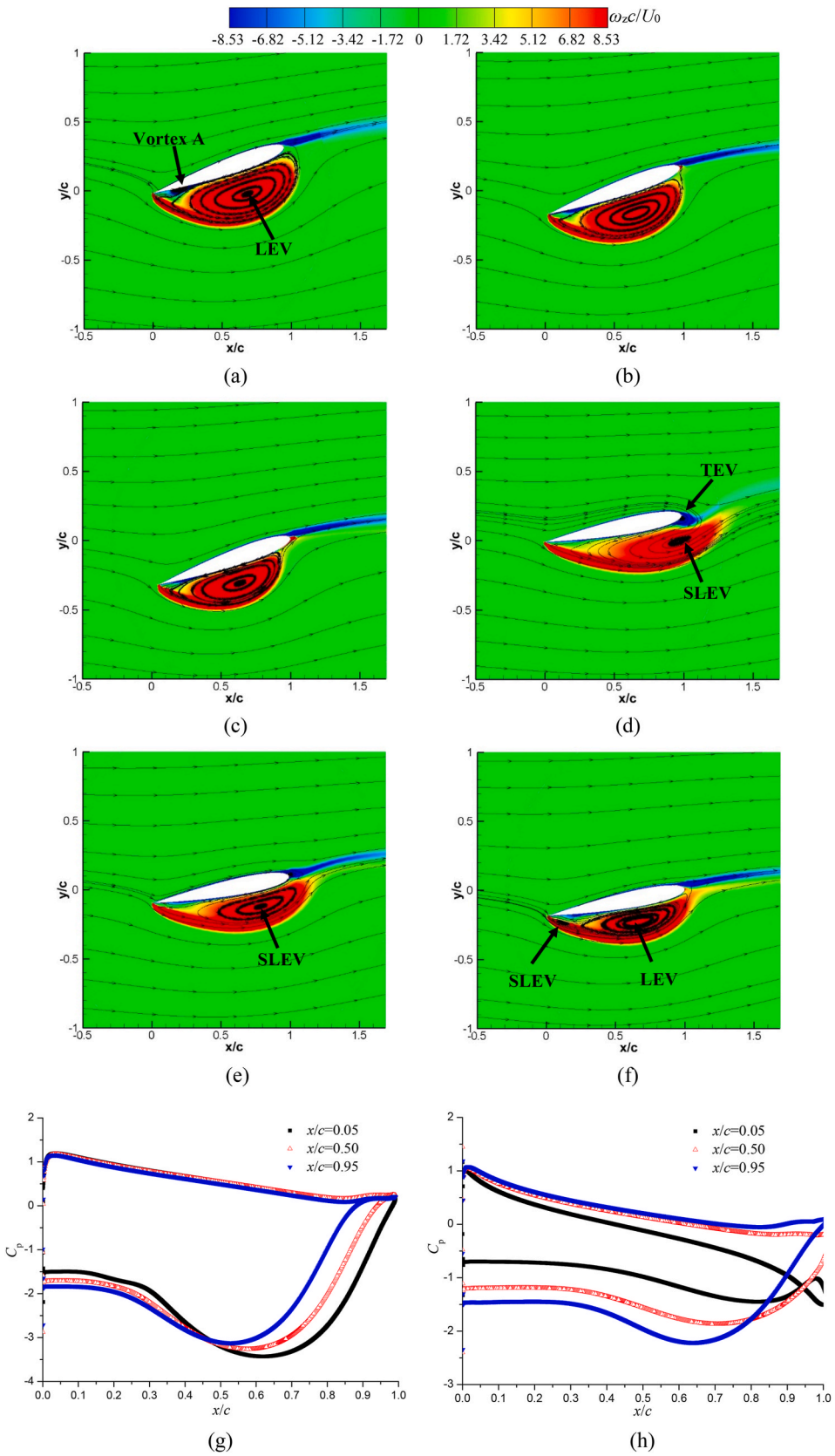

Fig. 15. Flow structures and pressure coefficients of airfoils with different pitching locations. (a), (b) and (c) $x/c = 0.05$, 0.50 and 0.95 at $t = 0.45T$; (d), (e) and (f) $x/c = 0.05$, 0.50 and 0.95 at $t = 0.73T$; (g) $t = 0.45T$; (h) $t = 0.73T$.

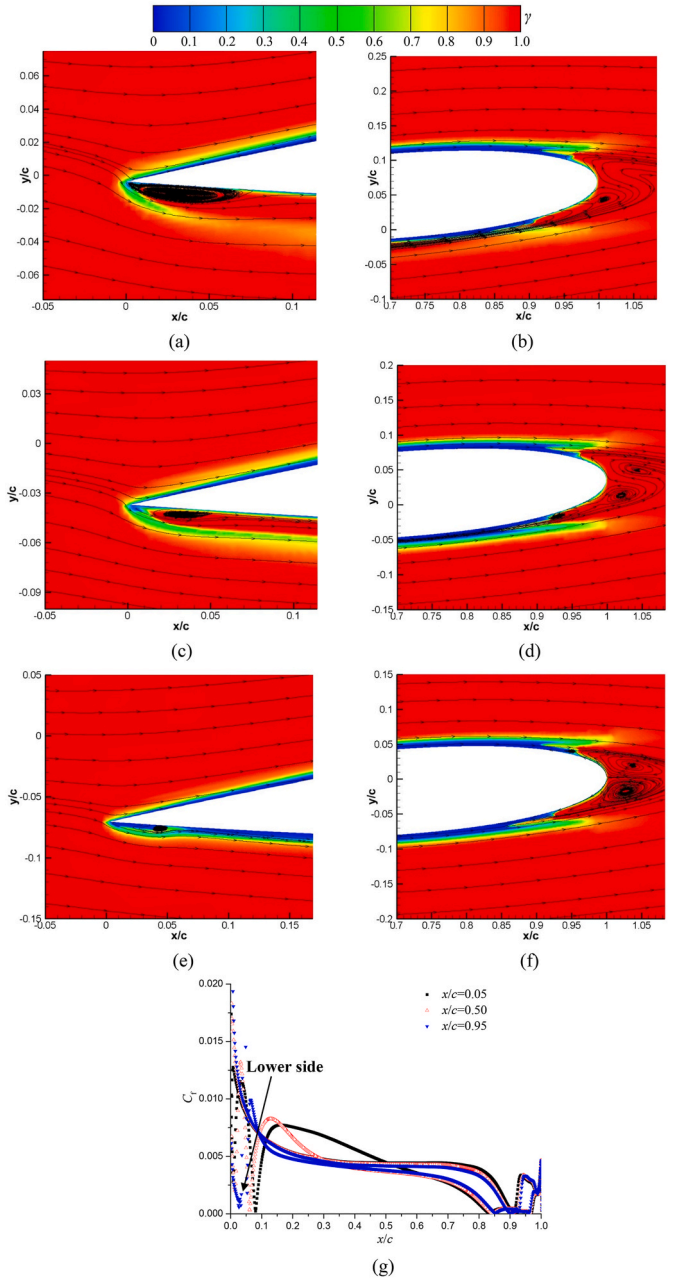

Fig. 16. Near-wall flows and skin friction coefficients of airfoils with different pitching locations. (a) and (b) $x/c = 0.05$ at $t/T = 0.15$; (c) and (d) $x/c = 0.50$ at $t/T = 0.15$; (e) and (f) $x/c = 0.95$ at $t/T = 0.15$; (g) Skin friction coefficients.

starts to shed after $x/c = 0.9$. When it comes to the movement of SLEV, it is observed that it moves faster compared with that at $k = 0.16$ (the slope of the curves), especially for the case with large pitching amplitude, because of the large pitching rate. Consequently, it concludes that at two k, the LEV trajectory is totally different, while the motion of SLEV is very similar, but the convection speed varies.

3.3. *Effect of the pitch-pivot-point on the reverse flow*

To investigate the influence of the pitch-pivot-point on the performance and flow structure, five locations, namely $x/c = 0.05$, 0.25, 0.50, 0.75 and 0.95, are selected in this section. In Fig. 14, it seems that the instantaneous lift coefficient is delayed as the pitch-pivot-point moves towards the blunt TE. Simultaneously, the sub-peak of the lift coefficient at nearly $t = 0.70T$ has a slightly larger magnitude for the case with the pitching location closer to the blunt TE. Thus, in order to explain the performance difference at the same instant, two locations at $t = 0.45T$ and $0.73T$, corresponds to two peaks of the lift coefficient, are studied in the following part.

The flow structures and pressure distributions at two instants for cases with different pitching locations are described in Fig. 15. At $t = 0.45T$, the large-scale LEV attaches on the lower surface of the airfoil, leading to the obvious pressure drop. Consequently, the negative lift is generated. However, for different cases, it is observed that the influence of LEV is more intensive when the pitch-pivot-point is closer to the sharp LE, which leads to the largest value of the lift coefficient shown in Fig. 14. At the same time, for the case with $x/c = 0.05$, the vortex A with the negative vorticity is visible, but it is absent for other two cases. At $t = 0.73T$, the lift coefficient curve has a sub-peak, where the SLEV and TEV coexist for $x/c = 0.05$ and 0.50, but the SLEV starts to shed from the surface when the pitch-pivot-point is located near LE. As the pitching location is at $x/c = 0.95$, the LEV still attaches on the surface and the SLEV develops within the separated shear layer. This phenomenon indicates that the flow structure evolution is postponed when the pitching location moves towards TE. The pressure distribution in Fig. 15h shows that the attached LEV can bring about the pressure drop on the lower surface, and the shedding of the LEV along with the development of the TEV is the main contributor to the performance deterioration, as shown in Fig. 14.

When the pitching airfoil has a relatively small incidence, the transition on the surface is studied, as displayed in Fig. 16, using the distributions of the intermittency and skin friction coefficients. Near the sharp LE, the shear layer is separated, resulting in the generation of the separation bubble. After that, the separated flow would reattach on the lower surface. Then, as the flow reaches to the blunt TE, the secondary flow separation occurs, both on two sides. Obviously, when the pitching location is closer to LE, the size of the separation bubble is larger, which leads to the reattachment point more downstream, as shown in Fig. 16g. Near the TE, the flow separation point on the lower side is more upstream while it is more downstream on the upper side, for the case with $x/c = 0.05$. Under this circumstance, the wake flow is quite asymmetrical, and a pair of vortices gradually lost the stability. However, they are still clearly captured for the case with $x/c = 0.95$. In addition, in Fig. 16d and f, the small size of the vortex is also observed on the upper or lower surface, indicating that the vortical flow in the wake originates from the unstable boundary layer. In conclusion, the large-scale separation bubble near LE for the case with $x/c = 0.05$ is responsible for the relatively large negative lift coefficient shown in Fig. 14, and the wake flow is more unsteady due to the asymmetrical boundary layer on the TE.

Then, the trajectory of two main vortices, including LEV and SLEV, are plotted in Fig. 17 for cases with three different pitching locations. It can be seen that the LEV moves away from the horizontal axis as the airfoil undergoes the downstroke process, which is more obvious when the pitch-pivot-point is close to TE. However, for the movement of the SLEV, it is found that the SLEV convects along with the horizontal axis in the up-stroke stage, due to the inertia force. Additionally, because of the delayed flow structure, the LEV and SLEV shed earlier for the case with the pitching location close to LE. Furthermore, the trajectory of vortices also depends on the effective angle of the pitching airfoil, which is responsible for the postponed flow filed.

The mechanism of the delayed flow structure due to the change of the pitch-pivot-point is clarified in Fig. 18. The previous work (Tian et al., 2016b) stated that the pitching motion at any point can be divided into two parts: a pitching motion based on a point and a plunging motion as a function of the baseline pitching. In Fig. 18a, the velocity triangle near the sharp LE of the reversed airfoil is displayed, in which the effective angle-of-attack, characterized by the angle between the local velocity and blade chord line, is given by

$$-\alpha_{eff} = -\alpha + tan^{-1}\left(\frac{W_{LE,Y}}{U_0 + W_{LE,X}}\right) \quad (1)$$

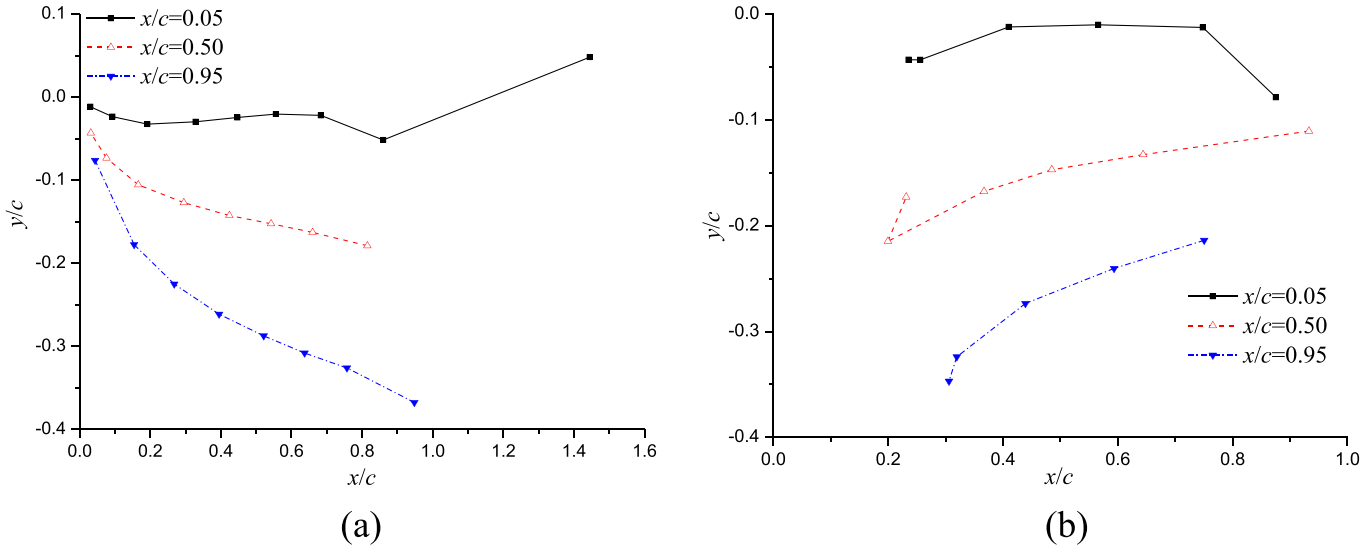

Fig. 17. Trajectory of LEV and SLEV of airfoils with different pitching locations. (a) LEV; (b) SLEV.

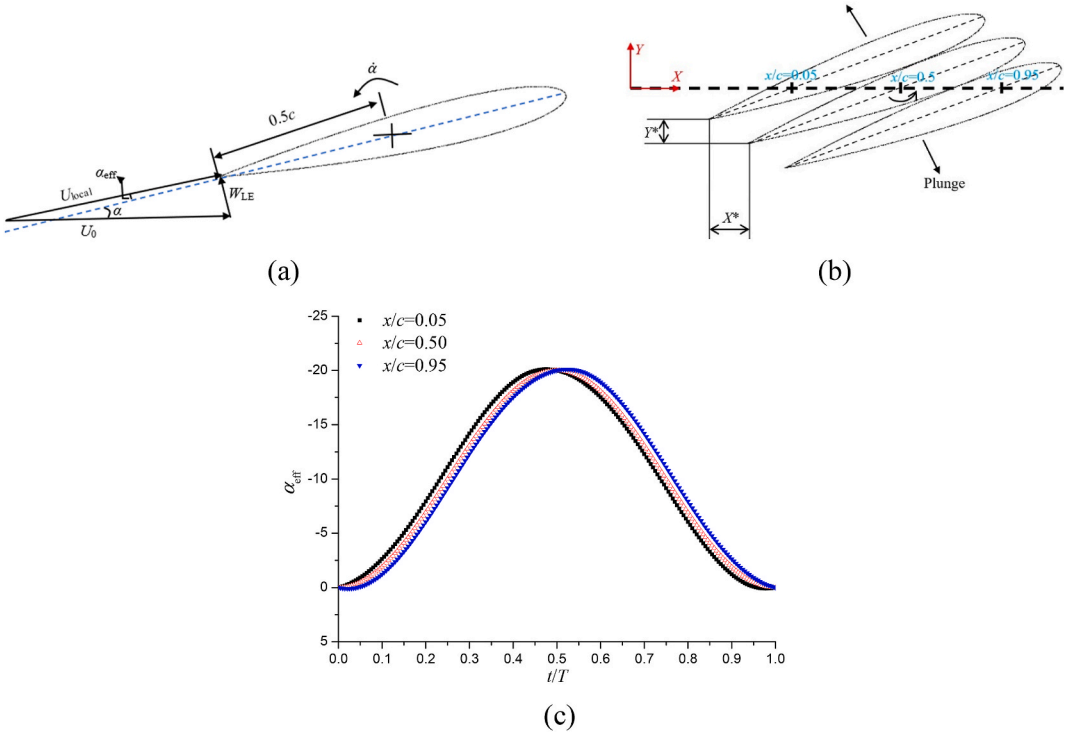

Fig. 18. Mechanism of the delayed flow structure of airfoils with different pitching locations. (a) Definition of the effective attack-of-angle; (b) Displacements in horizontal and vertical directions; (c) Distributions of the effective attack-of-angle.

In Fig. 18b, the original coordinate (X, Y) is defined when the airfoil has the incidence of 0°. Therefore, the pitching motion based on the pitch-pivot-point of $x/c = 0.05$ can be expressed as the pitching around $x/c = 0.50$ coupled with a plunging motion, with velocity components parallel and normal to the freestream flow. The displacements in horizontal and vertical directions: X^* and Y^*, for a pitching motion at any point which has a distance of x from the sharp LE is written as

$$X^* = \left(\frac{c}{2} - x\right)(cos\,\alpha - 1) \quad Y^* = \left(\frac{c}{2} - x\right) sin\,\alpha \tag{2}$$

The components of the relative velocity, namely $W_{LE,Y}$ and $W_{LE,X}$, can be obtained by differentiating the displacements with respect to time.

The distributions of the effective incidences for cases with different pitching locations are shown in Fig. 18c. It can be seen that during the down-stroke process, the maximal magnitude of the effective attack-of-angle appears earlier for the case with $x/c = 0.05$, which makes the contribution to the lift coefficient peak in Fig. 14. When the pitch-pivot-point is close to TE, the maximal effective incidence occurs at $t/T > 0.5$. In the up-stroke stage, the decrease of the effective incidence for the case with $x/c = 0.95$ is also slower compared with other two cases. In conclusion, based on the figures, it is clear that the postponed flow structure is determined by the effective incidence, which shows a phase shift when the pitching location moves towards TE. In the present work, the phase shift is not so evident, because of the relatively small k, which

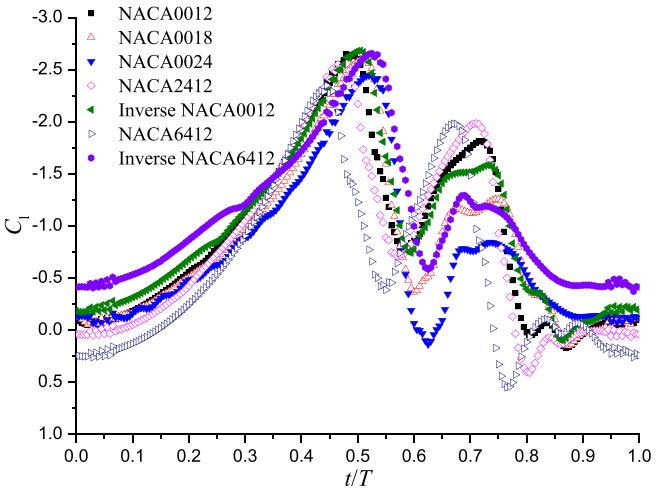

Fig. 19. Instantaneous lift coefficients of different blade profiles.

was also reported in references (Lind and Jones, 2016b; Seshadri et al., 2023).

3.4. *Effect of the blade camber on the reverse flow*

Previously, most work only consider the symmetrical profiles, for example, NACA00 series. With the consideration of the application to the wind turbines or propulsion devices, the influence of the blade profile should be investigated clearly. In this work, several blade shapes, including NACA0012, 0018, 0024, 2412 and 6412, as well as the inversed NACA2412 and NACA6412, are employed. Fig. 19 shows the instantaneous lift coefficient in a pitching cycle for different airfoils. With the increase of the airfoil thickness, the FMLC induced by LEV has a little bit delay. Additionally, the influence of SLEV on the performance at nearly $t/T = 0.7$ is more obvious, which shows that the intensity of SLEV becomes weak gradually. For asymmetrical blade profiles, it seems that the influence of LEV on the FMLC of NACA6412 is much weaker compared with NACA0012, and the location where the dynamic stall occurs is earlier. However, by the comparison with NACA0012, the SLEV produced by asymmetrical profiles has obvious impact on SMLC. When the asymmetrical airfoil is inversed, the variation of lift coefficient is totally different. For an example, the LEV is intensified while the SLEV is weakened for inverse NACA6412, compared with NACA6412. Simultaneously, the location of LEV is postponed evidently.

To analyze the influence of flow structure on the performance, four blade profiles, involving NACA0012, 0024, 6412 and inverse NACA6412, are adopted. Fig. 20 presents the near-wall flows at two locations where the maximal lift coefficient appears. According to the figures, it can be found that at FMLC, the LEV almost occupies the whole lower surface, but the LEV over NACA0024 is less influential than NACA0012, as shown in Fig. 20i. Moreover, the pressure distribution induced by LEV for NACA0024 and inverse NACA6412 is nearly the same. In Fig. 20b, the SLEV attaches on the lower surface, leading to the low pressure. However, due to the geometry curvature, the large-size SLEV on NACA6412 is visible, bringing about the lower pressure. For NACA0024 and inverse NACA6412, the SLEV is near LE, but the pressure difference on the aft part of NACA0024 is small, which results in the

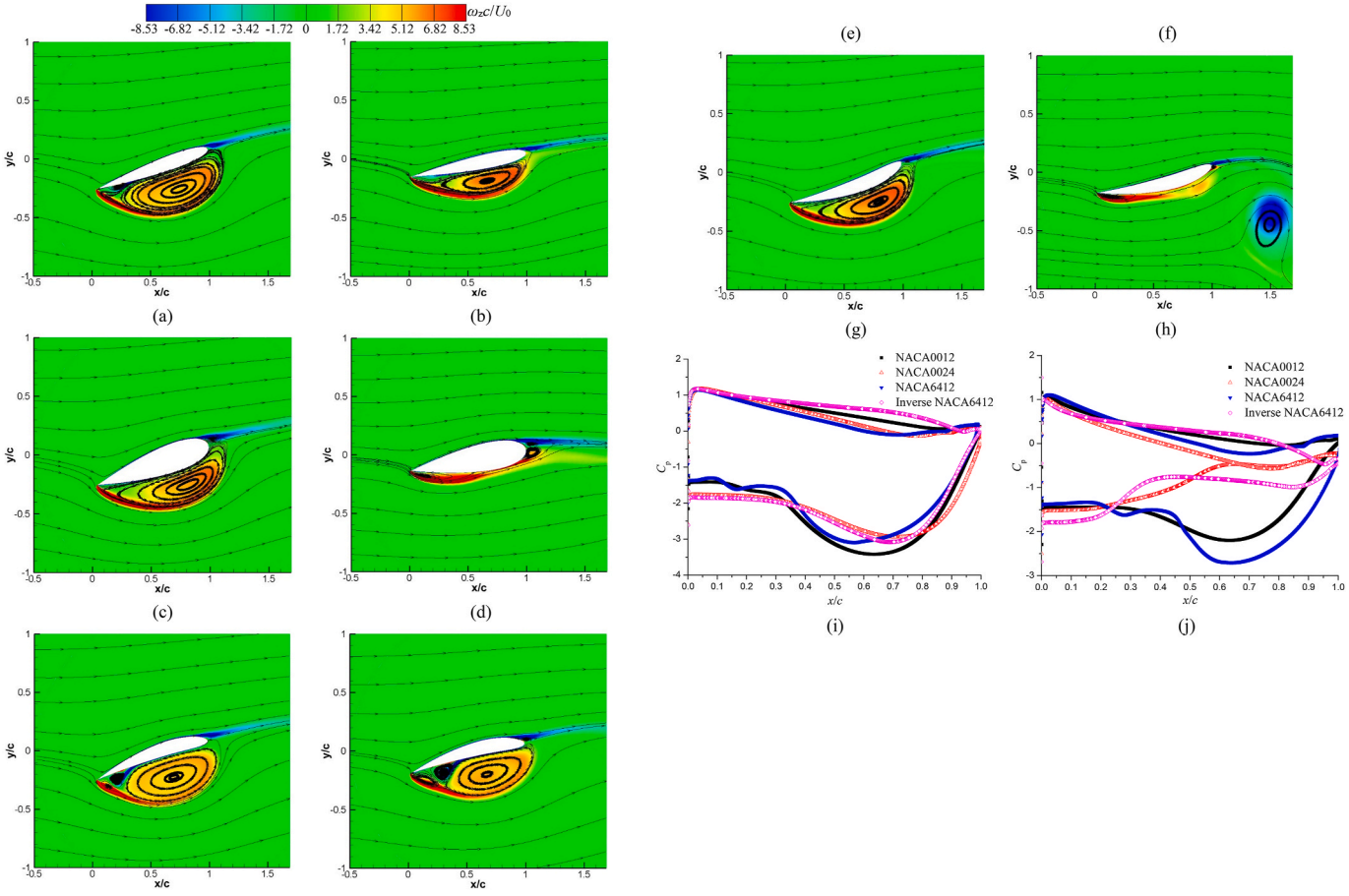

Fig. 20. Flow structures and pressure coefficients of different blade profiles. (a) and (b) NACA0012 at $t = 0.49T$ and $0.72T$; (c) and (d) NACA0024 at $t = 0.52T$ and $0.74T$; (e) and (f) NACA6412 at $t = 0.44T$ and $0.67T$; (g) and (h) Inverse NACA6412 $t = 0.52T$ and $0.69T$; (i) FMLC; (j) SMLC.

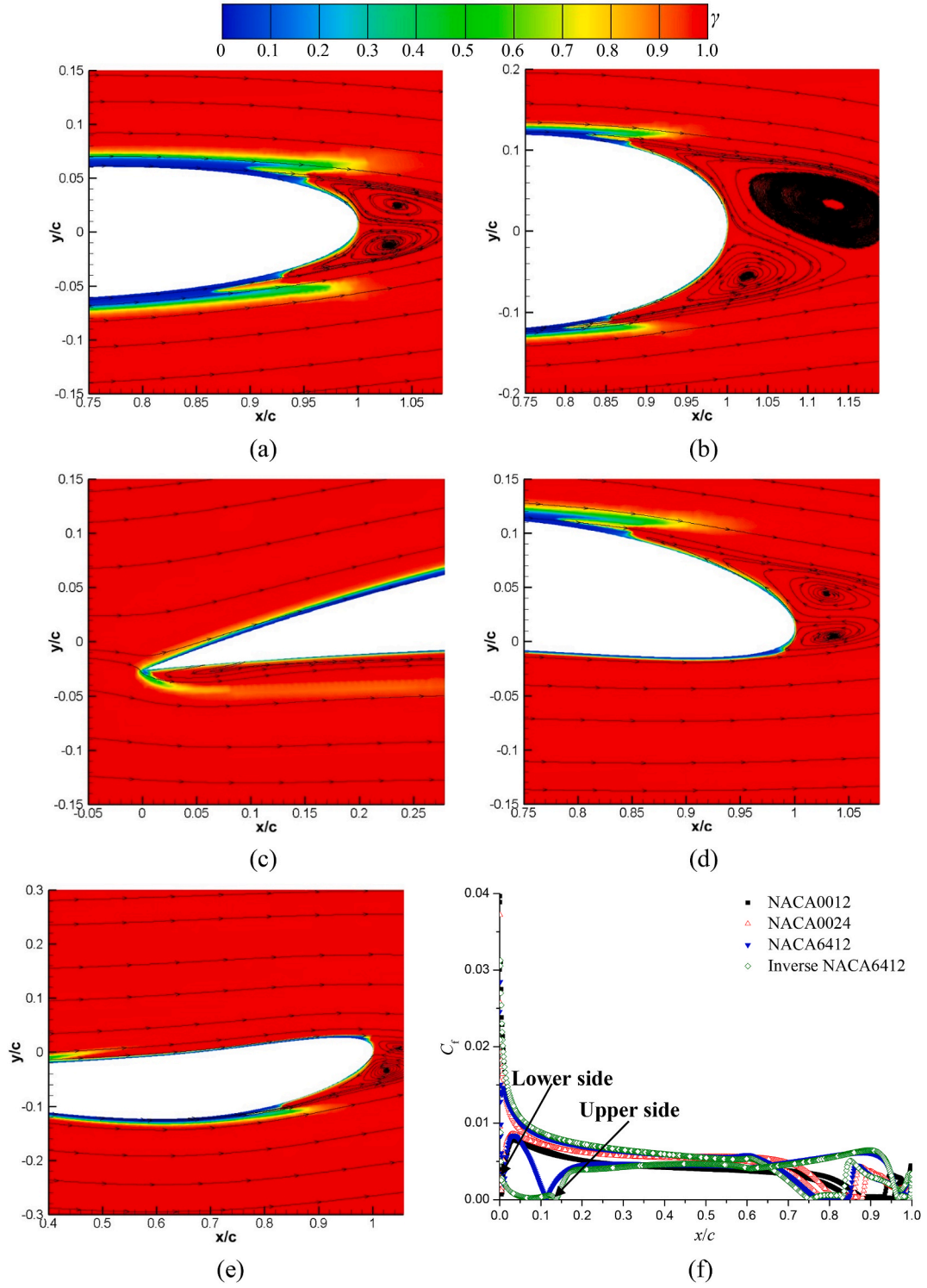

Fig. 21. Near-wall flows and skin friction coefficients of different blade profiles. (a) NACA0012 (TE); (b) NACA0024 (TE); (c) NACA6412 (LE); (d) NACA 6412 (TE); (e) Inverse NACA6412 (TE); (f) Skin friction coefficients.

relatively low lift coefficient. By the comparison of the pressure distribution in Fig. 20j, it concludes that the influence of SLEV on NACA6412 is more evident, because of the asymmetrical geometry that can produce the flow separation near the sharp LE easily.

The near-wall flow structures at relatively small incidence for different blade profiles are depicted in Fig. 21 using the distributions of the intermittency and skin friction coefficient. For the symmetrical airfoils, there is no flow separation occurring near the sharp LE. Near the TE, a pair of the vortices are visible, but the size is much larger for NACA0024. Moreover, although the boundary layer flow is almost symmetrical, the transition point of the thick airfoil is more upstream. Over the asymmetrical airfoil NACA6412, the flow separation appears near the sharp LE, and the shear layer transition is clear. Furthermore, the transition on the upper side near the TE is evident. However, for the inverse NACA6412, the transition on the upper surface is close to the LE while it approaches to the TE of the lower surface, leading to the extreme

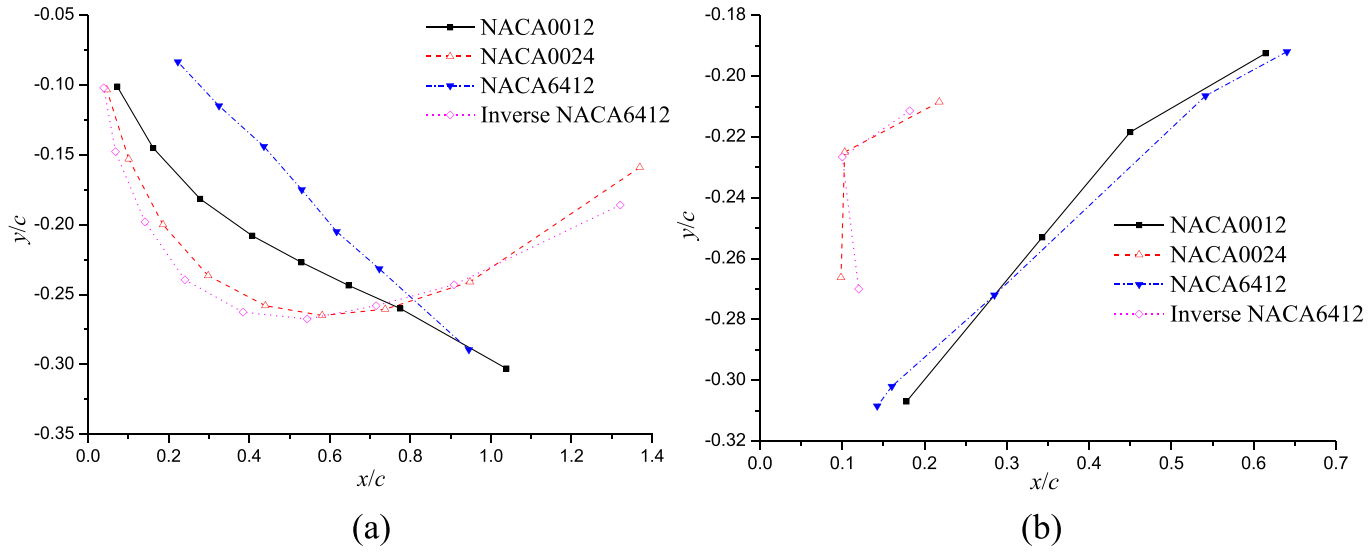

Fig. 22. Trajectory of LEV and SLEV of different blade profiles. (a) LEV; (b) SLEV.

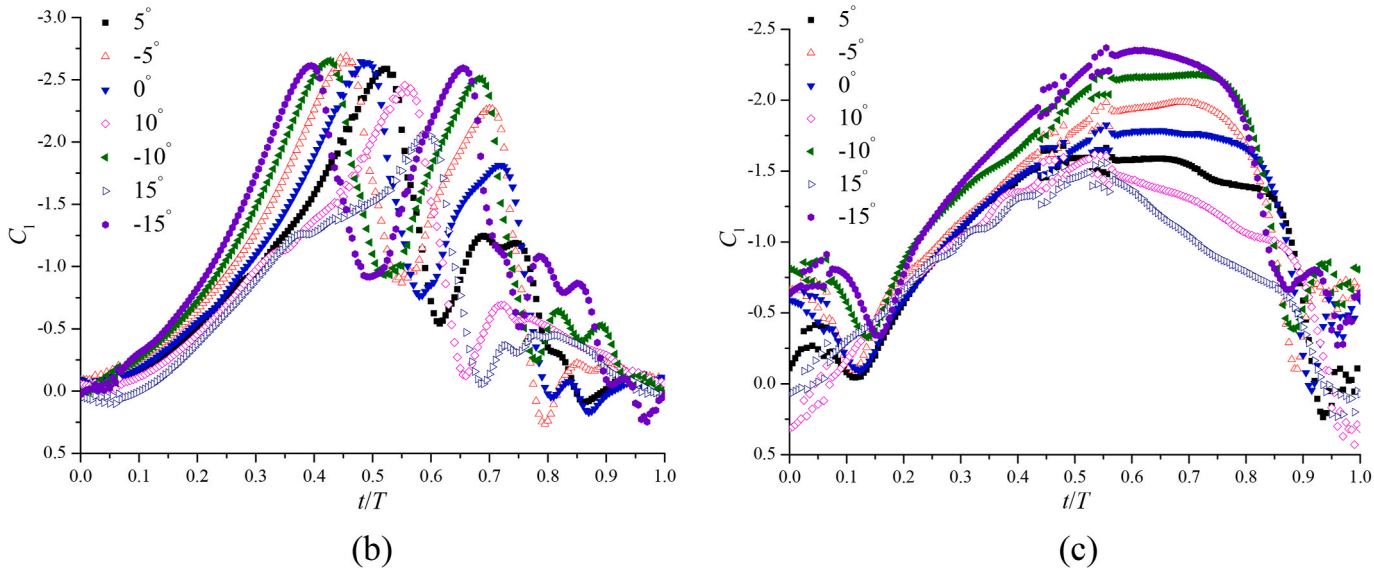

Fig. 23. Instantaneous lift coefficients of airfoils with different morphed angles. (a) Morphed LE; (b) $k = 0.16$; (c) $k = 0.50$.

asymmetrical boundary layer, further increasing the negative lift coefficient at $t/T = 0.1$, as shown in Fig. 19.

The trajectory of LEV and SLEV for different airfoils are plotted in Fig. 22. Regarding the trajectory of LEV, it is observed that the location is closer to the horizontal axis for NACA6412 due to the curvature effect. But the LEV motion is similar for NACA0012 and 6412, gradually leaving from the horizontal axis. At the same time, the movement of LEV over NACA0024 and inverse NACA6412 is nearly the same, firstly leaving the horizontal axis and then moving along it. In general, it seems that the LEV on NACA6412 separates earlier, and it is delayed for NACA0024 and inverse NACA6412, which can be inferred from Fig. 19. When it comes to the motion of SLEV, it can be seen that the trend is nearly the same for NACA0012 and 6412, and the SLEV always moves along the horizontal axis. However, for NACA0024 and inverse NACA6412, the SLEV is near the LE all the time in a pitching cycle, leading to the lower performance, which is shown in Fig. 19. Thus, it concludes that the blade profile has great impact on the motion of LEV and SLEV, especially for the thick symmetrical and inverse asymmetrical airfoils.

3.5. *Effect of the morphed leading edge on the reverse flow*

Several cases with different angles of the morphed LE, including -5°, 5°, 0°, 10°, -10°, -15° and 15°, are tested at two reduced frequency $k = 0.16$ and 0.50. The lift coefficients in a revolution are plotted in Fig. 23. At $k = 0.16$, when the sharp LE deflects downward, with the increase of the morphed angle, the occurrence of LEV is earlier, but the FMLC has the comparable magnitude. At the same time, the SMLC decreases, but it still larger than that of the airfoil without the morphed LE. When the LE bends upward, the LEV is delayed and the induced lift coefficient decreases with the increase of the morphed angle. The same trend is observed for the distribution of the maximal lift coefficient caused by the SLEV. As k increases to 0.50, the evident difference compared with that at $k = 0.16$ is that the deflected angle of the LE has great impact on the performance induced by LEV. Morphing upward decreases the negative lift coefficient while bending downward can increase it, which is the same trend for both LEV and SLEV.

To study the influence of the morphed LE on flow structures over the reversed pitching airfoils, the maximal lift coefficients induced by LEV

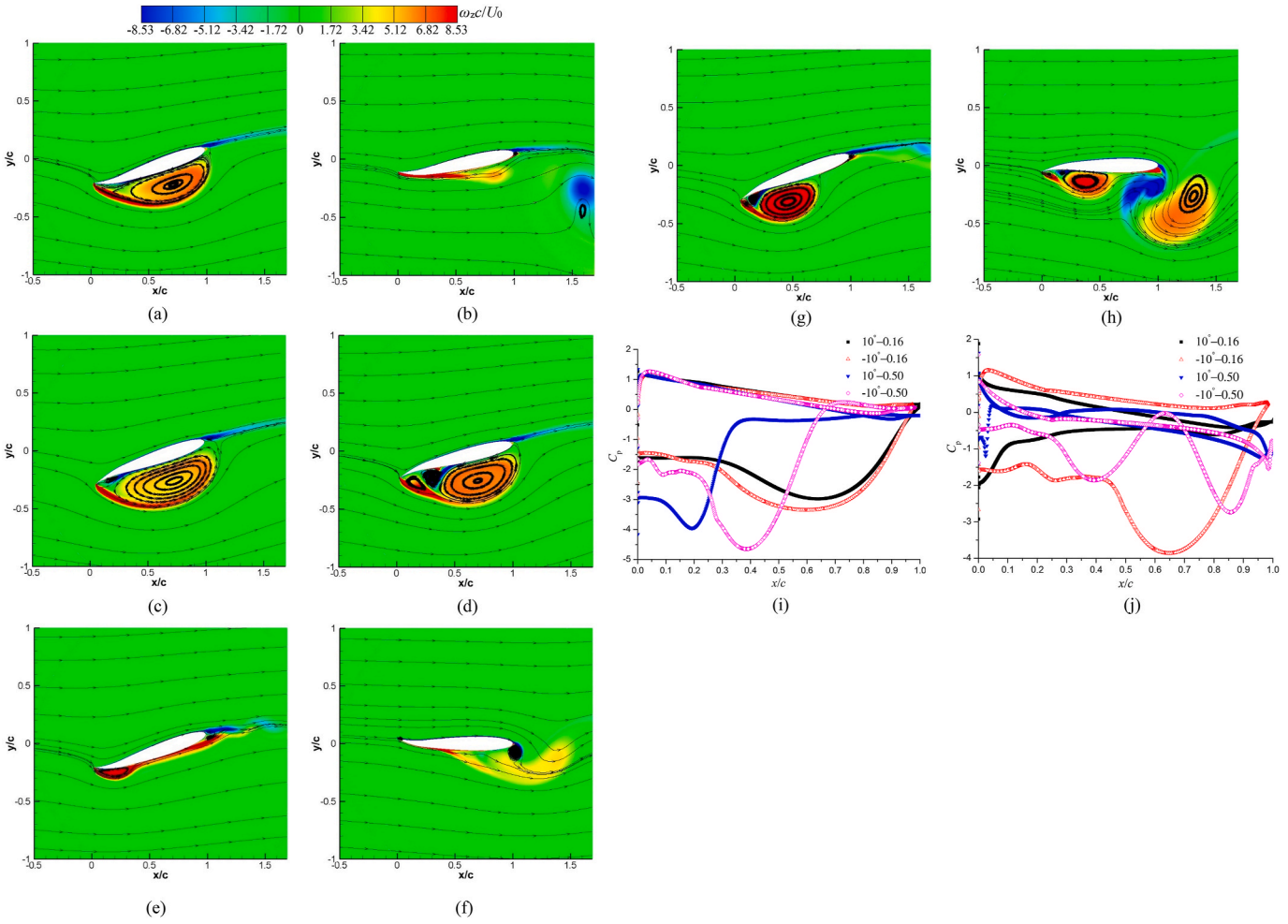

Fig. 24. Flow structures and pressure coefficients of airfoils with different morphed angles. (a) and (b) 10°-0.16 at $t = 0.55T$ and $0.72T$; (c) and (d) -10°-0.16 at $t = 0.42T$ and $0.68T$; (e) and (f) 10°-0.50 at $t = 0.55T$ and $1.0T$; (g) and (h) -10°-0.50 at $t = 0.55T$ and $0.94T$; (i) FMLC; (j) SMLC.

and SLEV for cases with morphed angles of 10° and -10° at $k = 0.16$ and 0.50 are analyzed. '10°-0.50' refers to the combination of the deflected angle with the reduced frequency k. In Fig. 24, when the LE deflects upward, the LEV generation is postponed. Although the LEV takes over the whole lower surface, the effect is more evident for the case with the LE morphing downward, as shown in Fig. 24i. As k increases from 0.16 to 0.50, the size of LEV becomes small and its location is closer to the LE. But the LEV over the airfoil in Fig. 24g has relatively large size, which has great impact on the pressure, due to the geometry curvature resulting in the flow separation easily. For the SMLC, it seems that the flow structure in Fig. 24b is simple and only the positive vorticity sheds from the lower surface. But when the LE deflects downward, except the LEV, the vortex A and TLEV are also visible, bringing about the low pressure on the suction side. As k increases, the pressure difference induced by the delayed flow structure is smaller than that at low k, for an instance, the TEV sheds into the wake in Fig. 24b while it still in the development in Fig. 24f. In conclusion, it is observed that the LE morphed downward can lead to the intensive flow separation, which is beneficial to maintain the low pressure on the lower side, further increasing the negative lift coefficient.

At relatively small incidence, the state of the near-wall flow is deserved to be investigated. The flow structures and skin friction coefficients for difference cases at $t/T = 0.1$ are displayed in Fig. 25. At $k = 0.16$, when the LE deflected upward, a small-size of LEV appears near the LE, and the separated shear layer induced transition is detected. After the LEV, the flow would reattach on the upper surface. However, with the increase of k, the occurrence of LEV is closer to the LE, and the reattachment point is more upstream. Simultaneously, near the TE, the main transition occurs on the lower surface, and a pair of vortices are clear, as shown in Fig. 25b. But in Fig. 25f, the separated shear layer emerges in the middle part of the lower surface, and the transition on the upper surface is closer to the TE. For the case with the LE morphed downward, due to the geometry curvature, a large-scale LEV appears, and the location of reattachment point is downstream with the increase of k. Near the blunt TE at two k, the transition is mainly on the upper side, but the location is upstream at low k, which is displayed in Fig. 25i. Moreover, it seems that the flow structure at $k = 0.50$ near the TE is more complex, characterized by the existence of the shedding LEV and trailing edge vortex.

Following the analysis of the boundary layer flow, the trajectory of LEV and SLEV for various cases are plotted in Fig. 26 at two k. It is noted that the SLEV over the airfoil with the LE deflected upward is not shown due to the location always close to the LE. Compared with the LE with a deflection of 10°, the trajectory of LEV at $k = 0.16$ is always away from the horizontal axis for other two cases. At $k = 0.50$, the trend of LEV for three cases is quite similar. However, when the LE is deflected downward, the LEV has a long distance from the horizontal axis and then moves towards it. When it comes to the motion of SLEV, it seems that it is nearly the same at $k = 0.50$. With the increase of k, the SLEV over the airfoil without deflected LE is closer to the horizontal axis. This event is due to the geometry curvature leading to the large flow separation near the LE with the deflection. Generally, it concludes that the path of LEV is greatly influenced by the morphed angle, regardless of k, while the motion of SLEV is significantly affected by increasing k.

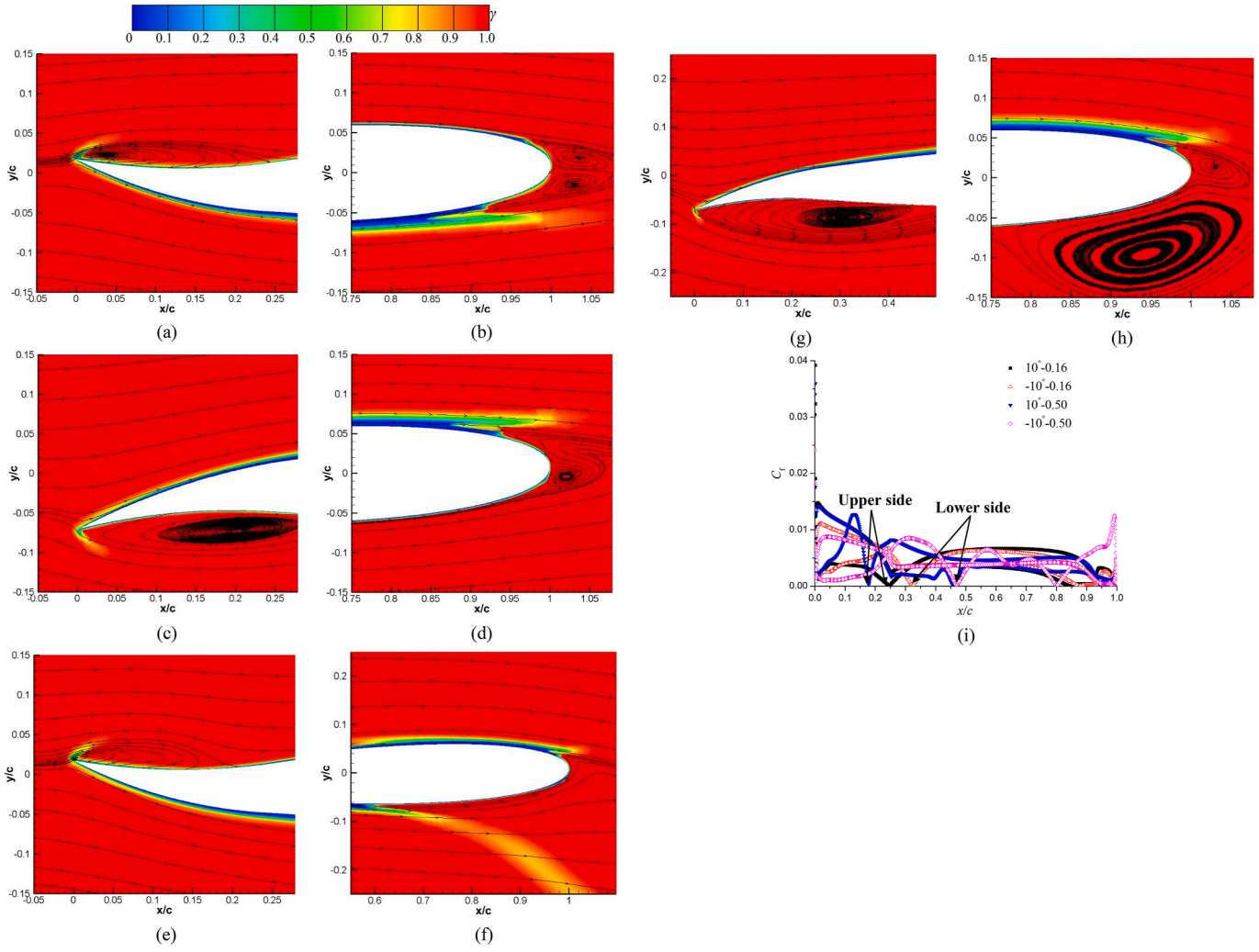

Fig. 25. Near-wall flows and skin friction coefficients of airfoils with different morphed angles. (a) and (b) 10°-0.16 (LE and TE); (c) and (d) −10°-0.16 (LE and TE); (e) and (f) 10°-0.50 (LE and TE); (g) and (h) −10°-0.50 (LE and TE); (i) Skin friction coefficients.

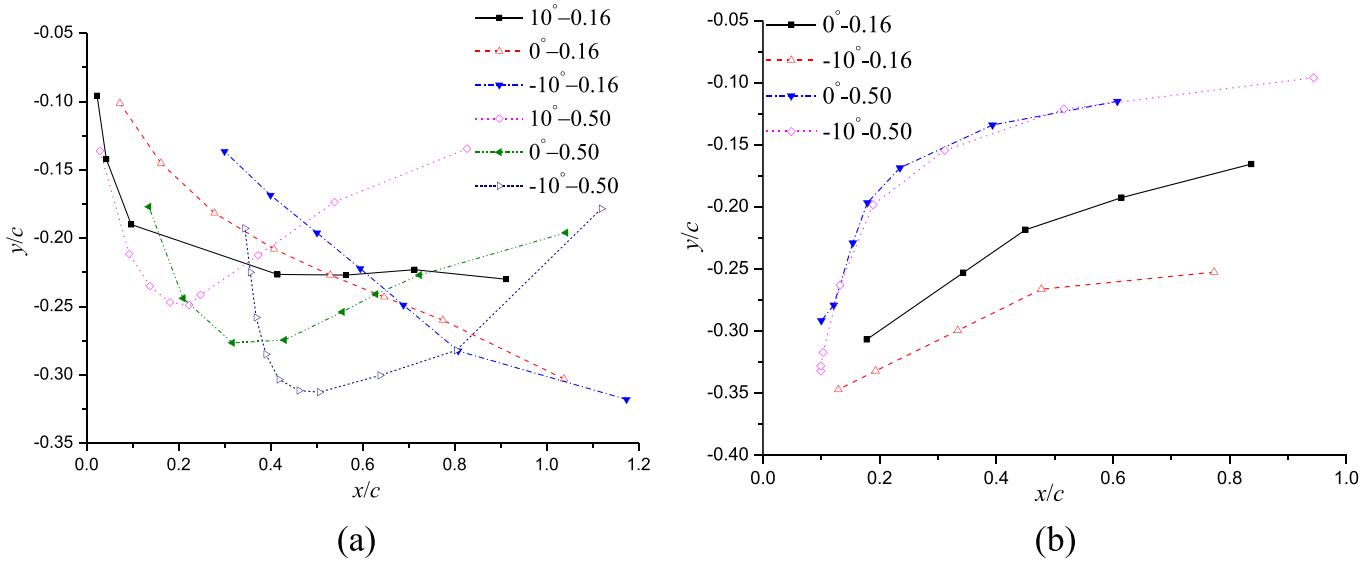

Fig. 26. Trajectory of LEV and SLEV of airfoils with different morphed angles at two *k*. (a) LEV; (b) SLEV.

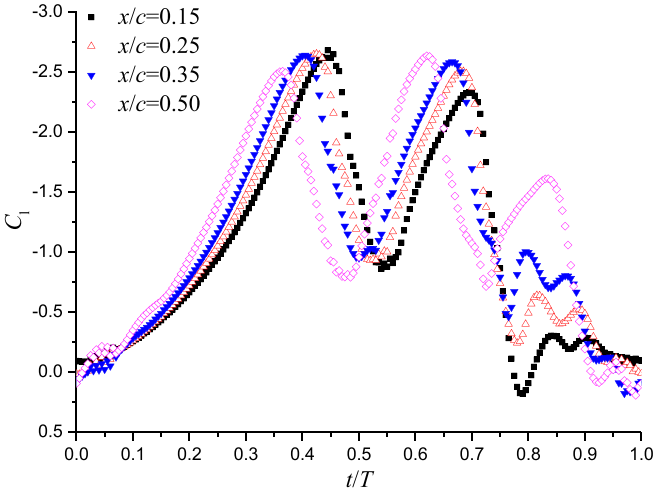

Fig. 27. Instantaneous lift coefficients of airfoils with different morphed positions.

The position where the LE starts to deflect is also a parameter that is deserved to be investigated. Thus, in this work, with a fixed deflection angle of 10°, various deflection locations, including $x = 0.15c$, $0.25c$, $0.35c$ and $0.50c$, are selected. At $k = 0.16$, the variation of lift coefficients for different cases in a pitching cycle is presented in Fig. 27. When the deflection position is close to the middle surface, the FMLC induced by LEV appears earlier, but the magnitude gradually decreases. However, for the SMLC induced by SLEV, it is observed that the value increases as the morphed position shifts towards the middle region. Furthermore, for the case with $x = 0.50c$, the third maximal lift coefficient (TMLC) is also evident at $t/T = 0.85$, which is ascribed to the generation of the TLEV.

The flow structures and pressure coefficients of airfoils with various deflection positions are shown in Fig. 28. When the deflection position moves towards the middle surface, the influence of LEV on the pressure along the lower surface becomes a little weak. At the same time, the vortex A with the negative vorticity beneath the LEV is absent in Fig. 28g. Except for the SLEV, the existence of TLEV and vortex A near the LE are also responsible for the SMLC, and this effect is more obvious for the LE deflected at position of $x/c = 0.50$. It is interesting that the SLEV in Fig. 28f has the largest impact on the pressure, which also leads to the comparable performance compared with that obtained by the airfoil with the deflection position at $x/c = 0.50$, as shown in Figs. 27 and 28j.

The transition near the blunt TE for tested cases with various morphed positions are displayed in Fig. 29, displayed by the distributions of intermittency and skin friction coefficients. It seems that the transition mainly occurs on the upper side, and its location is a little upstream when the deflection position is close to the middle surface. Simultaneously, a pair of vortices near the TE are visible for the case with $x/c = 0.15$, but it gradually disappears, as shown in Fig. 29d, because of the delayed flow field evolution. In Fig. 29e, near the sharp LE, the distribution of the skin friction coefficient shows that the

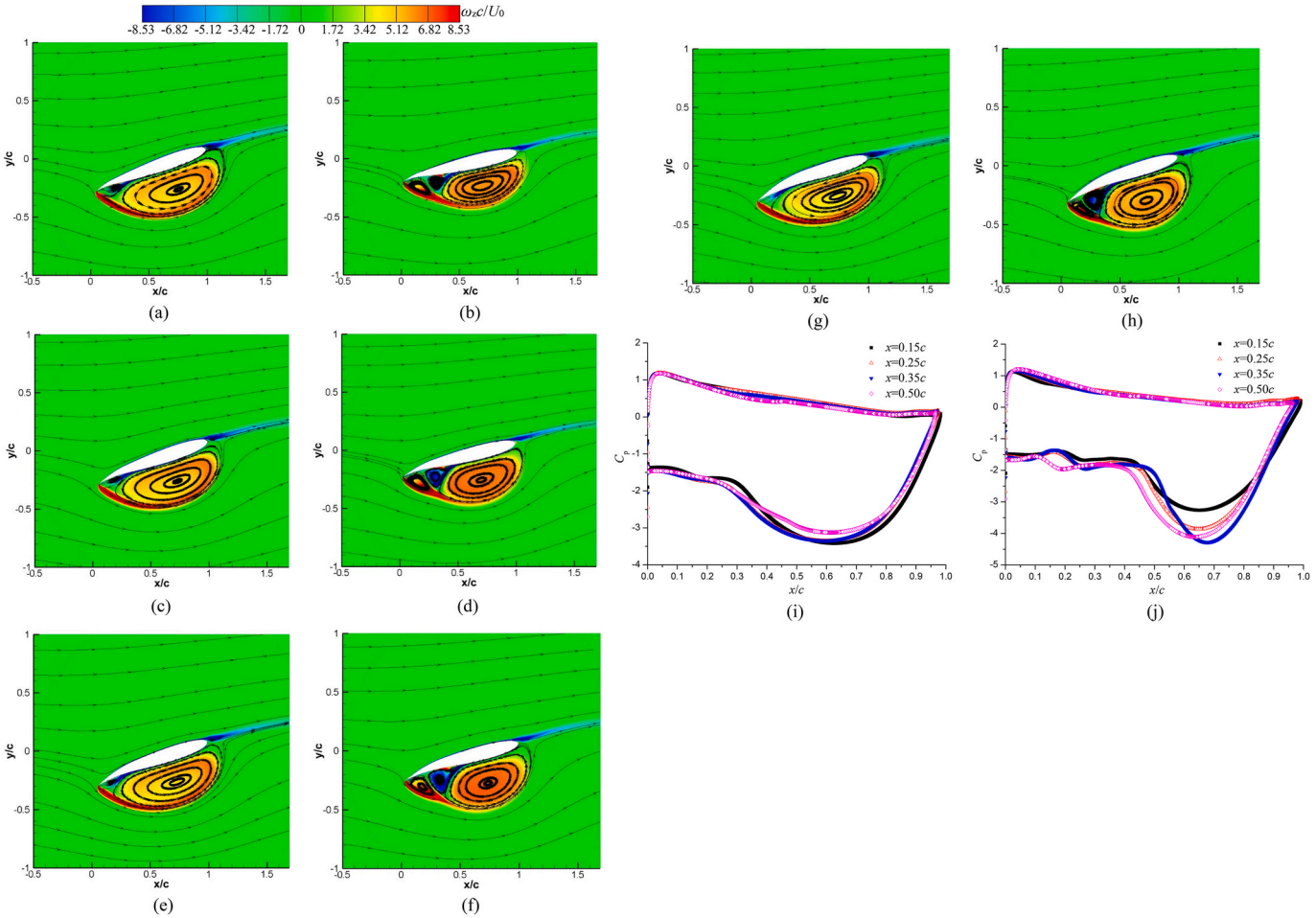

Fig. 28. Flow structures and pressure coefficients of airfoils with different morphed positions. (a) and (b) $x = 0.15c$ at $t = 0.45T$ and $0.70T$; (c) and (d) $x = 0.25c$ at $t = 0.42T$ and $0.68T$; (e) and (f) $x = 0.35c$ at $t = 0.40T$ and $0.67T$; (g) and (h) $x = 0.50c$ at $t = 0.36T$ and $0.62T$; (i) FMLC; (j) SMLC.

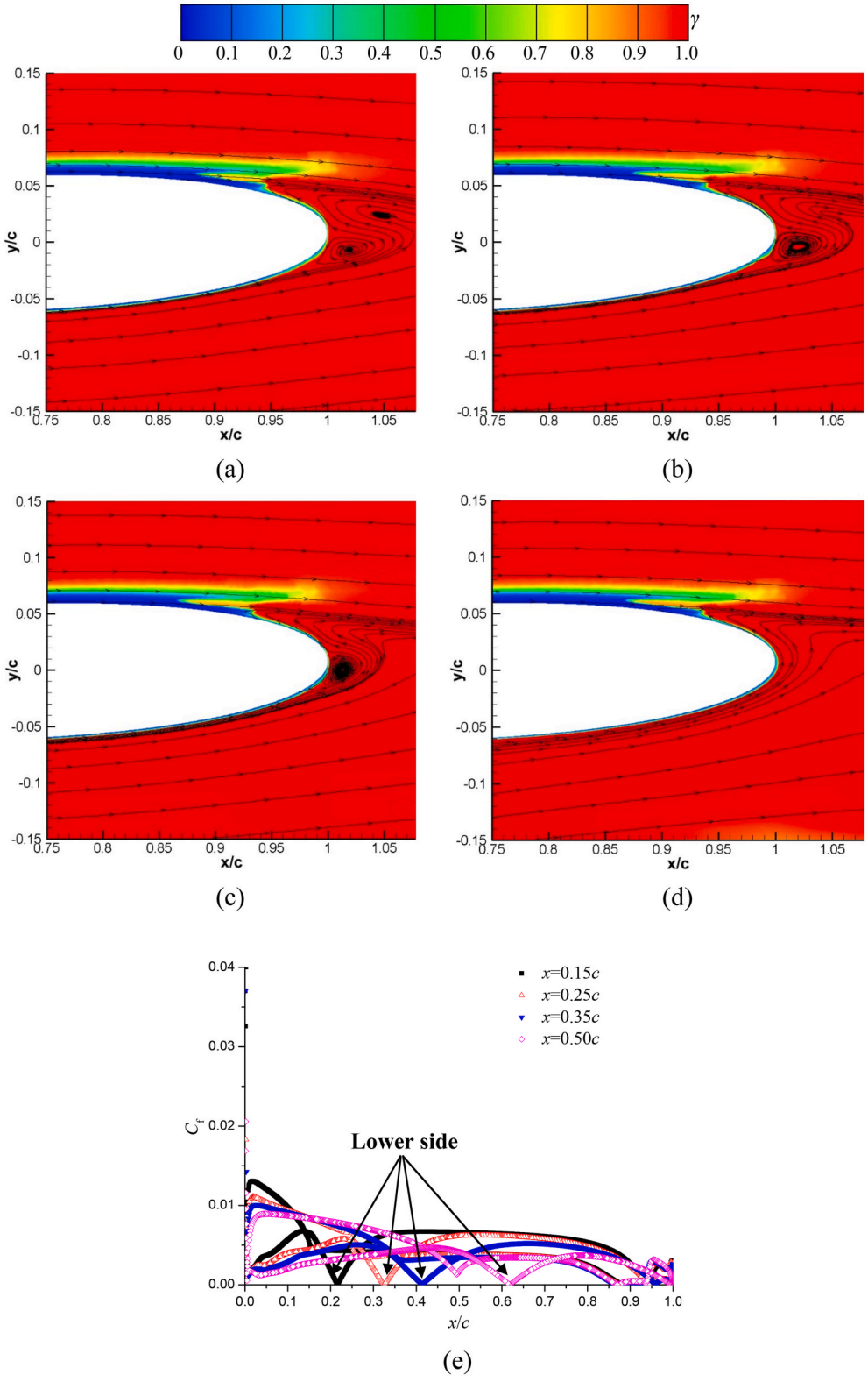

Fig. 29. Near-wall flows and skin friction coefficients of airfoils with different morphed positions. (a) $x = 0.15c$; (b) $x = 0.25c$; (c) $x = 0.35c$; (d) $x = 0.50c$; (e) Skin friction coefficients.

reattachment point of LEV is more downstream with the increase of the morphed position.

The trajectory of LEV and SLEV for different cases are plotted in Fig. 30 by tracing the vortex centre. The motion of LEV for airfoils with different morphed positions has no much difference, but the inception and shedding of LEV appear earlier. Moreover, the convection speed of LEV becomes large gradually based on the slope of the curves, when the morphed position is close to the middle surface. Regarding the movement of the SLEV, the general trend is that it moves along the horizontal axis, and then stays there for a while. However, the initial speed of SLEV

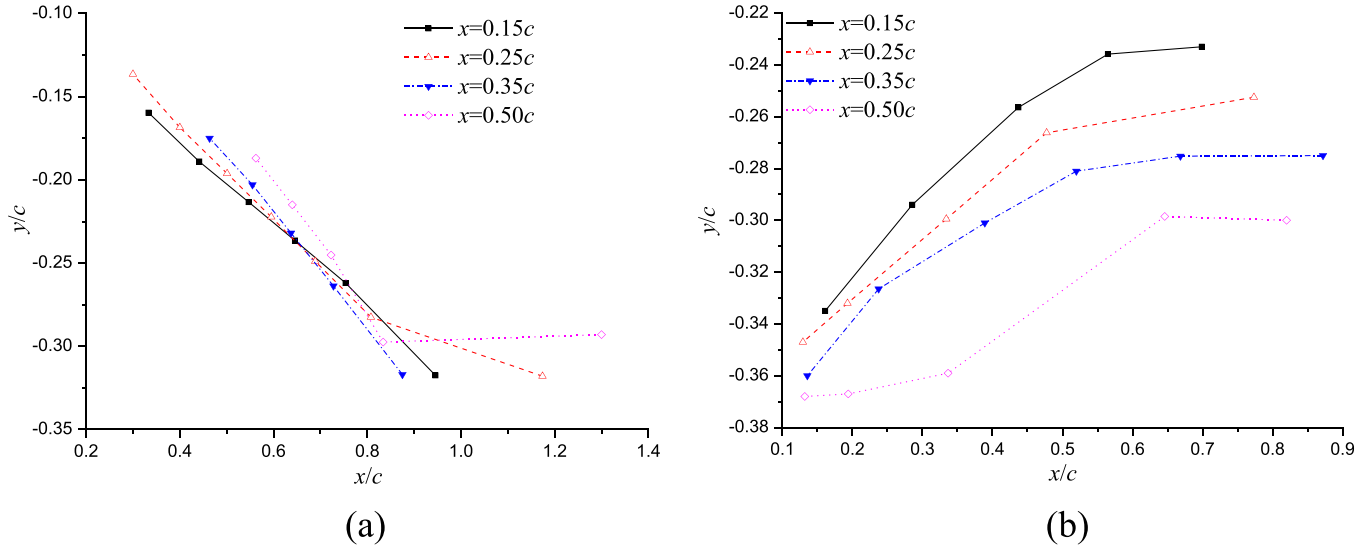

Fig. 30. Trajectory of LEV and SLEV of airfoils with different morphed positions. (a) LEV; (b) SLEV.

is relatively large for the airfoil with morphed position close to the LE. What is more, the SLEV over the airfoil with the deflection position of $x/c = 0.50$ has a small speed firstly, and then migrates quickly. As a result, the trajectory of SLEV is different from that in other three cases.

4. Concluding remarks

The SST $\gamma - \widetilde{Re}_{\theta t}$ transition model was adopted in this work to predict the performance and unsteady vortical flows over a revsered pitching airfoil. The main emphasis is on the influence of the pitching angle, pitch-pivot-point, blade camber and morphed LE on the instantaneous lift coefficient, boundary layer flow and trajectory of main vortices. The main conclusions are listed as follows:

(1) With the increase of k, the flow structure is delayed considerably, and the evolution of SLEV would appear in the next revolution. Regardless of k, increasing the mean pitching angle leads to the earlier generation of LEV and SLEV, as well as the intensity of these vortices. The transition over the surface includes the separated shear layer near the sharp LE and the flow separation near the blunt TE. Increasing k can delay the transition event. Simultaneously, the near-wall flow would become more complex with the increase of k, due to the existence of SLEV interacting with the wake flow. The trajectory of LEV is totally different for tested cases, especially at high k.

(2) Changing the pitch-pivot-point from LE to TE would make the performance and flow structures postponed. When the pitching location is close to LE, the size of LEV is larger, and the transition on the lower side at TE is more upstream while it is more downstream on the upper side. Because of the delayed effect, the LEV and SLEV shed into the wake earlier for the airfoil with the pitching point located near LE. Based on the theoretical analysis, the delayed flow structure can be explained by the distribution of the effective attack-of-angle.

(3) Increasing the symmetrical airfoil thickness, the magnitude of the maximal lift coefficients induced by LEV and SLEV decreases, especially for the latter. The LEV over NACA6412 has weak influence on the FMLC, while it has intensive effect on the second one. Simultaneously, the SMLC of the inverse NACA6412 is different from that of NACA0012. The boundary layer flow over the inverse NACA6412 is extremely asymmetrical. It is interesting that the trajectory of LEV and SLEV for NACA0012 and 6412 is quite similar, while they have nearly the same movement for NACA0024 and inverse NACA6412.

(4) With the increase of the morphed angle, the FMLC occurs earlier when the LE is deflected downward, while it is delayed and the magnitude becomes small gradually for airfoils with upward morphed LE. Then, the SMLC induced by SLEV becomes large for airfoils with downward LE, which is opposite for airfoils with upward LE. Due to the geometry curvature for the airfoil with downward deflected LE, the flow separation is intensive and the LEV has a large chance to interact with the wake flow. The path of LEV is greatly influenced by the morphed angle, regardless of k, while the motion of SLEV is significantly affected by increasing k.

(5) When the morphed position moves to LE, the performance and flow structure is postponed. The size of LEV is much larger as the morphed position shifts towards the middle surface. The morphed position has no much effect on the trajectory of LEV, but it has great influence on the movement of SLEV, especially for the airfoil with a deflection position of $x = 0.50c$.

CRediT authorship contribution statement

Lei Shi: Writing – original draft, Investigation. **Desheng Zhang:** Writing – review & editing, Supervision. **Annie-Claude Bayeul-Laine:** Software, Writing – review & editing. **Olivier Coutier-Delgosha:** Writing – review & editing, Supervision.

Declaration of competing interest

The authors declare that they have no known competing financial interests or personal relationships that could have appeared to influence the work reported in this paper.

Data availability

Data will be made available on request.

Acknowledgement

This work is financially supported by Senior Talent Fund Grant Project of Jiangsu University (5501440012).

References

Amiralaei, M.R., Alighanbari, H., Hashemi, S.M., 2010. An investigation into the effects of unsteady parameters on the aerodynamics of a low Reynolds number pitching airfoil. J. Fluid Struct. 26 (6), 979–993.

Benton, S.I., Visbal, M.R., 2018. Effects of leading-edge geometry on the onset of dynamic stall. AIAA J. 56 (10), 4195–4198.

Chao, L.M., Pan, G., Zhang, D., Yan, G.X., 2019. Numerical investigations on the force generation and wake structures of a nonsinusoidal pitching foil. J. Fluid Struct. 85, 27–39.

Cole, J.A., Vieira, B.A., Coder, J.G., Premi, A., Maughmer, M.D., 2013. Experimental investigation into the effect of Gurney flaps on various airfoils. J. Aircraft 50 (4), 1287–1294.

Durbin, P.A., 1993. A Reynolds stress model for near-wall turbulence. J. Fluid Mech. 249, 465–498.

Granlund, K., Ol, M., Bernal, L., 2011. Flow field evolution vs. lift coefficient history for rapidly-pitching low aspect ratio plates. In: 6th AIAA Theoretical Fluid Mechanics Conference, p. 3118.

Guillaud, N., Balarac, G., Goncalvès, E., 2018. Large eddy simulations on a pitching airfoil: analysis of the reduced frequency influence. Comput. Fluids 161, 1–13.

Hansen, K.L., Kelso, R.M., Dally, B.B., 2011. Performance variations of leading-edge tubercles for distinct airfoil profiles. AIAA J. 49 (1), 185–194.

Hillenherms, C., Schröder, W., Limberg, W., 2004. Experimental investigation of a pitching airfoil in transonic flow. Aero. Sci. Technol. 8 (7), 583–590.

Hodara, J., Lind, A.H., Jones, A.R., Smith, M.J., 2016. Collaborative investigation of the aerodynamic behavior of airfoils in reverse flow. J. Am. Helicopter Soc. 61 (3), 1–15.

Jacobellis, G., Gandhi, F., Rice, T.T., Amitay, M., 2020. Computational and experimental investigation of camber-morphing airfoils for reverse flow drag reduction on high-speed rotorcraft. J. Am. Helicopter Soc. 65 (1), 1–14.

Kim, D.H., Chang, J.W., 2014. Low-Reynolds-number effect on the aerodynamic characteristics of a pitching NACA0012 airfoil. Aero. Sci. Technol. 32 (1), 162–168.

Kirk, T.M., Yarusevych, S., 2017. Vortex shedding within laminar separation bubbles forming over an airfoil. Exp. Fluid 58 (5), 1–17.

Ko, D., Guha, T.K., Amitay, M., 2021. Control of reverse flow over a cantilevered blade using passive camber morphing. AIAA J. 59 (12), 5310–5331.

Kundu, P., 2020. Numerical simulation of the effects of passive flow control techniques on hydrodynamic performance improvement of the hydrofoil. Ocean. Eng. 202, 107108.

Li, X., Feng, L.H., Li, Z.Y., 2019. Flow mechanism for the effect of pivot point on the aerodynamic characteristics of a pitching airfoil and its manipulation. Phys. Fluids 31 (8), 087108.

Lind, A.H., Jones, A.R., 2015. Vortex shedding from airfoils in reverse flow. AIAA J. 53 (9), 2621–2633.

Lind, A.H., Jones, A.R., 2016a. Unsteady airloads on static airfoils through high angles of attack and in reverse flow. J. Fluid Struct. 63, 259–279.

Lind, A.H., Jones, A.R., 2016b. Unsteady aerodynamics of reverse flow dynamic stall on an oscillating blade section. Phys. Fluids 28 (7), 077102.

Lind, A.H., Lefebvre, J.N., Jones, A.R., 2014. Time-averaged aerodynamics of sharp and blunt trailing-edge static airfoils in reverse flow. AIAA J. 52 (12), 2751–2764.

Lind, A.H., Smith, L.R., Milluzzo, J.I., Jones, A.R., 2016. Reynolds number effects on rotor blade sections in reverse flow. J. Aircraft 53 (5), 1248–1260.

Lu, K., Xie, Y.H., Zhang, D., 2013. Numerical study of large amplitude, nonsinusoidal motion and camber effects on pitching airfoil propulsion. J. Fluid Struct. 36, 184–194.

Mamouri, A.R., Lakzian, E., Khoshnevis, A.B., 2019. Entropy analysis of pitching airfoil for offshore wind turbines in the dynamic stall condition. Ocean. Eng. 187, 106229.

Marchand, J.B., Astolfi, J.A., Bot, P., 2017. Discontinuity of lift on a hydrofoil in reversed flow for tidal turbine application. Eur. J. Mech. B Fluid 63, 90–99.

Martinat, G., Braza, M., Hoarau, Y., Harran, G., 2008. Turbulence modelling of the flow past a pitching NACA0012 airfoil at 10^5 and 10^6 Reynolds numbers. J. Fluid Struct. 24 (8), 1294–1303.

McCroskey, W.J., McAlister, K.W., Carr, L.W., Pucci, S.L., Lambert, O., Indergrand, R.F., 1981. Dynamic stall on advanced airfoil sections. J. Am. Helicopter Soc. 26 (3), 40–50.

Menter, F.R., Kuntz, M., Langtry, R., 2003. Ten years of industrial experience with the SST turbulence model. Turbulence, Heat and Mass Transfer 4 (1), 625–632.

Menter, F.R., Langtry, R.B., Likki, S.R., Suzen, Y.B., Huang, P.G., Völker, S., 2006a. A correlation-based transition model using local variables—part I: model formulation. J. Turbomach. 128, 413–422.

Menter, F.R., Langtry, R., Völker, S., 2006b. Transition modelling for general purpose CFD codes. Flow, Turbul. Combust. 77 (1), 277–303.

Rahromostaqim, M., Posa, A., Balaras, E., 2016. Numerical investigation of the performance of pitching airfoils at high amplitudes. AIAA J. 54 (8), 2221–2232.

Rezaeiha, A., Montazeri, H., Blocken, B., 2019. On the accuracy of turbulence models for CFD simulations of vertical axis wind turbines. Energy 180, 838–857.

Seshadri, P.K., Aravind, A., De, A., 2023. Leading edge vortex dynamics in airfoils: effect of pitching motion at large amplitudes. J. Fluid Struct. 116, 103796.

Seshagiri, A., Cooper, E., Traub, L.W., 2009. Effects of vortex generators on an airfoil at low Reynolds numbers. J. Aircraft 46 (1), 116–122.

Seyhan, M., Akbıyık, H., Sarıoğlu, M., Keçecioğlu, S.C., 2022. The effect of leading-edge tubercle on a tapered swept-back SD7032 airfoil at a low Reynolds number. Ocean. Eng. 266, 112794.

Shi, L., Wang, Y., Zhang, D., Bayeul-Lainé, A.C., Coutier-Delgosha, O., 2022. Parametrical study on separation-induced transition and vortex dynamics of a reversed pitching airfoil. Ocean. Eng. 264, 111665.

Shur, M.L., Strelets, M.K., Travin, A.K., Spalart, P.R., 2000. Turbulence modeling in rotating and curved channels: assessing the Spalart-Shur correction. AIAA J. 38 (5), 784–792.

Tian, W., Bodling, A., Liu, H., Wu, J.C., He, G., Hu, H., 2016a. An experimental study of the effects of pitch-pivot-point location on the propulsion performance of a pitching airfoil. J. Fluid Struct. 60, 130–142.

Tian, W., Bodling, A., Liu, H., Wu, J.C., He, G., Hu, H., 2016b. An experimental study of the effects of pitch-pivot-point location on the propulsion performance of a pitching airfoil. J. Fluid Struct. 60, 130–142.

Tseng, C.C., Hu, H.A., 2016. Flow dynamics of a pitching foil by Eulerian and Lagrangian viewpoints. AIAA J. 54 (2), 712–727.

Wang, J.J., Li, Y.C., Choi, K.S., 2008. Gurney flap—lift enhancement, mechanisms and applications. Prog. Aero. Sci. 44 (1), 22–47.

Wu, X., Zhang, X., Tian, X., Li, X., Lu, W., 2020. A review on fluid dynamics of flapping foils. Ocean. Eng. 195, 106712.

Yu, H.T., Bernal, L.P., 2017. Effects of pivot location and reduced pitch rate on pitching rectangular flat plates. AIAA J. 55 (3), 702–718.

Zhang, M., Wu, Q., Wang, G., Huang, B., Fu, X., Chen, J., 2020. The flow regime and hydrodynamic performance for a pitching hydrofoil. Renew. Energy 150, 412–427.